Economic Geology, v. 116, no. 4, pp. 883–907

New Insights into the Origin of the World-Class Jinding Sediment-Hosted Zn-Pb Deposit, Southwestern China: Evidence from LA-ICP-MS Analysis of Individual Fluid Inclusions

Lan Mu,[1,2] Ruizhong Hu,[1,2,†] Xianwu Bi,[1] Yongyong Tang,[1] Tingguang Lan,[1] Qin Lan,[1] Jingjing Zhu,[1] Jiantang Peng,[1] and Abiola Oyebamiji[1]

[1]*State Key Laboratory of Ore Deposit Geochemistry, Institute of Geochemistry, Chinese Academy of Sciences, Guiyang 550081, China*

[2]*College of Earth and Planetary Sciences, University of Chinese Academy of Sciences, Beijing 100049, China*

Abstract

The Jinding deposit in the Lanping basin, southwest China, is the largest sandstone-hosted Zn deposit in the world and the second largest Zn-Pb deposit in China. However, questions related to the metal compositions and origin of the ore fluids remain. In this study, microthermometry and laser ablation-inductively coupled plasma-mass spectrometry (LA-ICP-MS) were employed to determine the properties and compositions of individual fluid inclusions trapped in sphalerite and calcite. The results show that the fluid inclusions trapped in sphalerite and calcite have similar homogenization temperatures (79°–173°C with the majority 100°–130°C), salinities (10.3–29.1 wt % NaCl + $CaCl_2$ equiv with the majority 24.5–27.4 wt % NaCl + $CaCl_2$ equiv), and concentrations of alkali and alkali earth elements (e.g., Na, Ca, Mg, K, Sr, Ba, Li, Rb, and Cs). However, the concentrations of ore and associated metals (e.g., Pb, Sb, Ag, and Tl) in the fluid inclusions hosted by sphalerite are significantly higher than those hosted by calcite. Based on these observations, we propose that the sulfides including sphalerite were precipitated from a low-temperature, high-salinity, Ca-rich, metal-rich fluid, while the gangue minerals such as calcite crystallized subsequently from fluids depleted in metals due to prior precipitation of sulfides, and that the high salinities of the fluid inclusions are likely due to a combination of seawater evaporation and subsequent dissolution of evaporitic sequences during fluid percolation. The LA-ICP-MS analyses reveal that the fluid inclusions have K/Na, Rb/Na, and Cs/Na ratios within the range of modern basinal brines, and Li/Na, Ba/Na, and Ca/Na ratios share similar compositions with the ore fluids of basement interacted deposits in the world. The Jinding ore fluids contain ~200 to 650 ppm Pb, based on the data of fluid inclusions trapped in sphalerite. The estimated concentrations of Zn in the ore fluids are also very high at ~200 to 6,500 ppm. Our results reveal that anomalously metal rich fluids played a critical role in the formation of the giant Jinding sediment-hosted Pb-Zn deposit. We concur with the previous suggestion that sulfide precipitation at Jinding occurred when ascending metal-rich brines encountered an H_2S-rich, Ca-rich fluid, which was produced by interaction of hydrocarbons with evaporites, in the cap of the Jinding dome.

Introduction

Sediment-hosted Pb-Zn deposits, which are mainly associated with siliciclastic and carbonate rocks and typically have no direct genetic association with igneous activity, represent the most important repositories of Pb and Zn on Earth (Leach et al., 2005, 2010). The two main classes of sediment-hosted Pb-Zn deposits—sedimentary exhalative (SEDEX) and Mississippi Valley-type (MVT) deposits—contain approximately half the global resources of Zn and Pb (Singer, 1995; Wilkinson, 2014). However, the genesis of some giant Pb-Zn deposits is poorly constrained. Determining the composition of ore fluids, including the metal concentrations, major element concentrations, and available reduced sulfur, provides an important way to understand ore-forming processes. Recent laser ablation-inductively coupled plasma-mass spectrometry (LA-ICP-MS) studies of individual fluid inclusions have proposed that metal contents of ore fluids can greatly exceed those measured in almost all modern brines, and thus ore formation might be linked to the influx of anomalously metal rich fluids (Stoffell et al., 2004, 2008; Wilkinson et al., 2009; Appold and Wenz, 2011; Wenz et al., 2012; Pelch et al., 2015). However, there is the possibility that some anomalously high Zn and Pb concentrations could result from the ablation of accidental solid inclusions, thereby yielding data that may not represent the true compositions of the aqueous phase (Hammerli et al., 2013; Pelch et al., 2015; Field et al., 2020). In addition, the metal contents of fluid inclusions in nonsulfide minerals may differ from those in sulfide-hosted fluid inclusions, which implies that they were precipitated from different fluids, or at least at different stages of the paragenesis. Thus, important questions remain about the metal concentrations of ore fluids in sediment-hosted Pb-Zn deposits that need to be addressed by further analyses, including comparison between different minerals.

The Sanjiang metallogenic belt contains a variety of economically valuable sediment-hosted Pb-Zn deposits that share some similarities with typical MVT ore deposits (He et al., 2009; Liu et al., 2017). The Jinding deposit, located in the Lanping basin, is one of the largest and best-known deposits in the Sanjiang metallogenic belt. It has a total reserve of ~220 million tonnes (Mt) of ore with average grades of 6.1 wt % Zn and 1.3 wt % Pb (Third Geological Team, 1984). Previous fluid inclusion studies on the deposit were hampered by the small size of many of the inclusions. Reported microthermometric results (Wen et al., 1995; Xue et al., 2007; Tang et al., 2011; Chi et al., 2017) indicate a wide range of homogenization temperatures (40°–370°C) and salinities (1.2–18 wt % NaCl equiv). These relatively poorly constrained properties have

[†]Corresponding author: e-mail, huruizhong@vip.gyig.ac.cn

ISSN 0361-0128; doi:10.5382/econgeo.4826; 25 p.
Digital appendices are available in the online Supplements section.

Submitted: January 9, 2020 / Accepted: October 12, 2020

hindered understanding of ore genesis at Jinding. Two main models for the genesis of the deposit have been proposed over the last few decades, including epigenetic hydrothermal origins (Gao, 1989; Qin and Zhu, 1991; Hu et al., 1998; Kyle and Li, 2002; Chi et al., 2007, 2017; Xue et al., 2007; Tang et al., 2014; Leach et al., 2017) and syngenetic origins with posthydrothermal overprinting (Shi et al., 1983; Bai et al., 1985; Wu and Wu, 1989; Zhao, W.Y., 1989; Zhao, Z., 2007; Zeng et al., 2016). Some studies have also suggested that the Jinding deposit may represent a new type of sediment-hosted Pb-Zn deposit, distinct from the typical MVT and SEDEX classes (Xue et al., 2007; Wang et al., 2009). Thus, the genesis of the deposit remains under debate, especially regarding the origin of the ore fluids, models for which include (1) mantle-derived fluids, based on noble gas isotopes and the presence of CO_2-rich fluid inclusions (Teng et al., 2000; Xue et al., 2003, 2007; Li et al., 2011), (2) sedimentary brines, based on the occurrence of evaporites and nearby saline springs or Na-Ca-Cl-SO_4 compositions of fluid inclusions as determined by crush-leach techniques (Shi et al., 1983; Qin and Zhu, 1991; Luo et al., 1994; Wen et al., 1995; Kyle and Li, 2002; Tang, 2013), and (3) meteoric fluids, based on studies of noble gas, hydrogen, and oxygen isotopes (Hu, 1998; Tang et al., 2013). It should be pointed out that the different conclusions are mainly based on different researchers' data including He-Ar and Pb isotopes. Therefore, more systematic studies of fluid inclusions are still needed.

Fluid inclusions are the most direct and representative samples of ore fluids. They can reveal the nature of the fluids and can be used to trace fluid origins and evolution. Advances in LA-ICP-MS analysis technology enable direct quantitative determination of the compositions of individual fluid inclusions with a high spatial resolution and with low detection limits (Gunther et al., 1998; Heinrich et al., 1999, 2003; Allan et al., 2005; Guillong et al., 2008; Seo et al., 2011; Pettke et al., 2012). LA-ICP-MS analysis of fluid inclusions has been successfully applied to numerous deposits and has provided new insights into their origins, such as the sources of ore-forming fluids and solutes, and mineralization processes (e.g., Audetat et al., 1998, 2000; Stoffell et al., 2004, 2008; Klemm et al., 2007; Kouzmanov et al., 2010; Smith et al., 2013; Simpson et al., 2015; Large et al., 2016; Lan et al., 2018; Liu et al., 2018).

Using the LA-ICP-MS technique, we have determined the compositions of individual fluid inclusions trapped in hydrothermal sphalerite and calcite crystals from the world-class Jinding Zn-Pb deposit. Prior to this, systematic studies on fluid inclusion assemblages (FIAs), cathodoluminescence (CL), petrography, and microthermometry were conducted to characterize the fluid inclusions and provide necessary constraints for the LA-ICP-MS analysis. The objective of this study is to obtain accurate information on the composition of ore fluids and to gain new insights into the origin of the word-class Jinding Zn-Pb deposit.

Geologic Setting

The Jinding Zn-Pb deposit is located in the Sanjiang Tethyan domain in southwestern China (Fig. 1a). The Sanjiang Tethyan domain, which extends for nearly 2,000 km along the eastern margin of the Tibetan Plateau, was formed by the amalgamation of Gondwana-derived microcontinental blocks and arc terranes as a result of Tethyan oceanic subduction and Indo-Asian continental collision from the Paleozoic to Cenozoic (Mo et al., 1994; Metcalfe, 2002, 2013; Deng et al., 2014b; Wang et al., 2014). A series of basins developed in the Sanjiang region due to rifting and postcollisional extension during the Late Triassic. These basins, such as the Changdu, Lanping, and Simao basins, have similar sedimentary sequences and tectonic evolutionary histories (Fig. 1b; Tao et al., 2002; Pan et al., 2003).

The Lanping basin, located on the southern margin of the Sanjiang Tethys domain, is bounded by the Changning-Menglian suture to the west and the Jinshajiang and Ailaoshan sutures to the east (Fig. 1b; Wu et al., 1995; Wang et al., 2014). Middle to Late Triassic bimodal arc volcanic rocks and volcano-sedimentary strata, thought to be related to the subduction of the Paleo-Tethyan Ocean beneath the Asian continent, are exposed on the eastern and western rims of the basin (Fig. 1c; Mo et al., 1994; Yang et al., 2014). The interior of the basin is filled by thick Mesozoic to Cenozoic sedimentary sequences. Upper Triassic marine limestones, clastic rocks, and sandy mudstones deposited over 1,600 m in the rift basin (Luo et al., 1994; Tao et al., 2002). The overlying Jurassic-Cretaceous strata are mainly composed of continental sedimentary rocks such as red beds, interbedded with minor carbonates, which are thought to have been deposited in a foreland basin (Mou et al., 1999; Yin and Harrison, 2000). From the Paleogene to Neogene, lacustrine clastic sedimentary rocks, including siltstone, mudstone, sandstone, and conglomerate, were deposited in the basin (Mou et al., 1999). The basement of the basin is composed of Precambrian gneiss, amphibolite, sericite schist, and marble, which are exposed in some places along the basin margins (Yunnan Bureau Geological Mineral Resource, 1990).

Evaporites, mainly gypsum and anhydrite, are commonly associated with the Late Triassic carbonate sequences, the Middle Jurassic red beds, and the Paleocene red beds. This indicates a long-term arid environment in the Lanping basin, which was most important during the early Paleogene when thick evaporite sequences formed (Yunnan Bureau Geological Mineral Resource, 1990; Gao, 1991). Discordant gypsum bodies, with flow textures and containing Late Triassic limestone clasts, have been interpreted to be the products of halokinesis (Leach et al., 2017).

The India-Asia continental collision during the Cenozoic (started ca. 55–50 Ma; Dupont-Nivet et al., 2010; Najman et al., 2010) caused intense extrusion and shortening in the northern Sanjiang region and rotation and extension in the south (Tapponnier et al., 1990; Chen et al., 1995; Chung et al., 1997; Wang et al., 2001; Spurlin et al., 2005). Mesozoic strata were strongly folded and thrusted into nappes that now overlie the Neogene sequences (Mo et al., 1994; Yin and Harrison, 2000; He et al., 2009). The thrust faults are cut by large-scale, NS-trending, strike-slip fault systems, which contain an array of brittle fault surfaces with nearly westerly dip that underwent early-stage sinistral and late-stage dextral strike-slip shearing (Tapponnier et al., 1990; Liu et al., 2004; Spurlin et al., 2005). The Cenozoic collision was accompanied by tectonic-magmatic-metallogenic activity in the Sanjiang orogenic belt, producing some porphyry Cu-Au deposits, sediment-hosted Pb-Zn deposits, and orogenic Au deposits (Fig. 1b; Ye

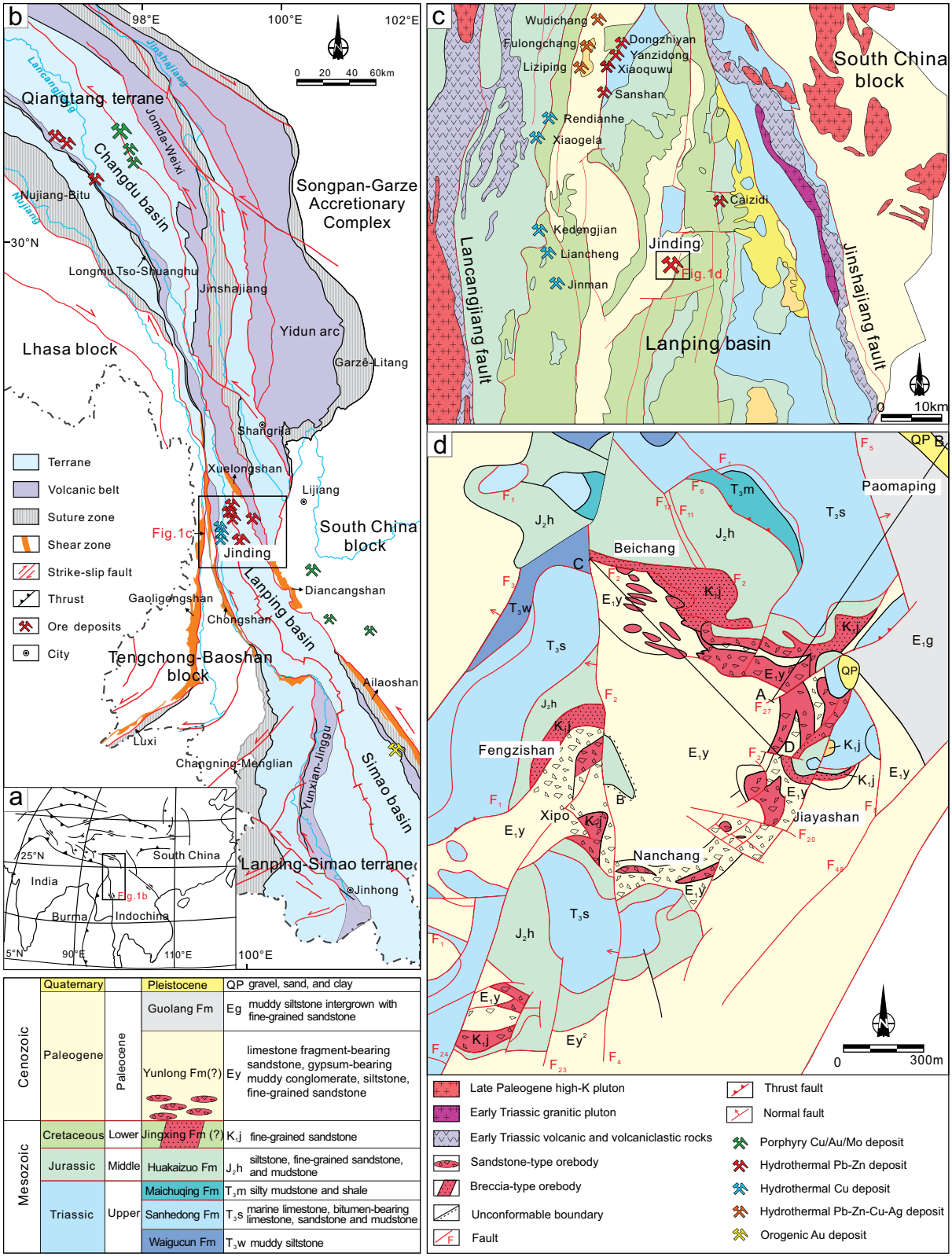

Fig. 1. Regional and local geology of the Jinding deposit. (a) Simplified map of eastern Asia showing the location of the study area (modified after Yin and Harrison., 2000). (b) Geologic map of the Sanjiang Tethyan orogen showing the major tectonic units and structural traces (modified after Deng et al., 2014a). (c) Geologic map of the northern Lanping basin showing the structural control of the deposit (modified after Third Geological Team, 1984). (d) Geologic map of the Jinding Zn-Pb deposit showing the geology and distribution of ores in the Jinding dome (modified after Tang et al., 2014). A-B and C-D indicate the locations of the cross sections in Figure 2.

et al., 1992; Hou et al., 2007; Song et al., 2011; Deng et al., 2014b; Bi et al., 2019). Potassic felsic stocks (~42–32 Ma) are present along the strike-slip faults on the margins of the Lanping basin (Chung et al., 1998; Wang et al., 2001). A few felsic stocks (~39–36 Ma) are present within the basin (Zhang et al., 2000; Dong et al., 2005), but no igneous rocks have been found in the Jinding area.

Deposit Geology and Mineralogy

Deposit geology

The Jinding Zn-Pb deposit is hosted within a tectonic dome that extends over 8 km². The stratigraphic sequence is cut by an overthrust fault (F2) and can be divided into a lower autochthonous sequence and an upper, older, allochthonous klippe (Fig. 1d). The autochthonous succession consists of the Paleocene Yunlong and Guolang Formations, which are composed of siltstone, fine-grained sandstone, limestone fragment-bearing sandstone, and evaporitic mudstones. The allochthonous succession consists of the Upper Triassic Maichuqing, Sanhedong, and Waigucun Formations, the Middle Jurassic Huakaizuo Formation, and the Lower Cretaceous Jingxing Formation. The Upper Triassic sedimentary sequence is mainly composed of marine limestone, dark-gray bituminous limestone, and mudstone. The Huakaizuo Formation is composed of siltstone, sandstone, and mudstone. The Jingxing Formation is composed of fine-grained, gray sandstone (Figs. 1d, 2).

A NNE-trending normal dip-slip fault (F27), which is regarded as a branch of the Bijiang fault system by some researchers (Chi et al., 2006, 2007), appears to have controlled the distribution of orebodies at Jinding. The limited results of thermochronology (Li et al., 2000) and paleomagnetic dating (Yalikun et al., 2017) suggest that mineralization took place

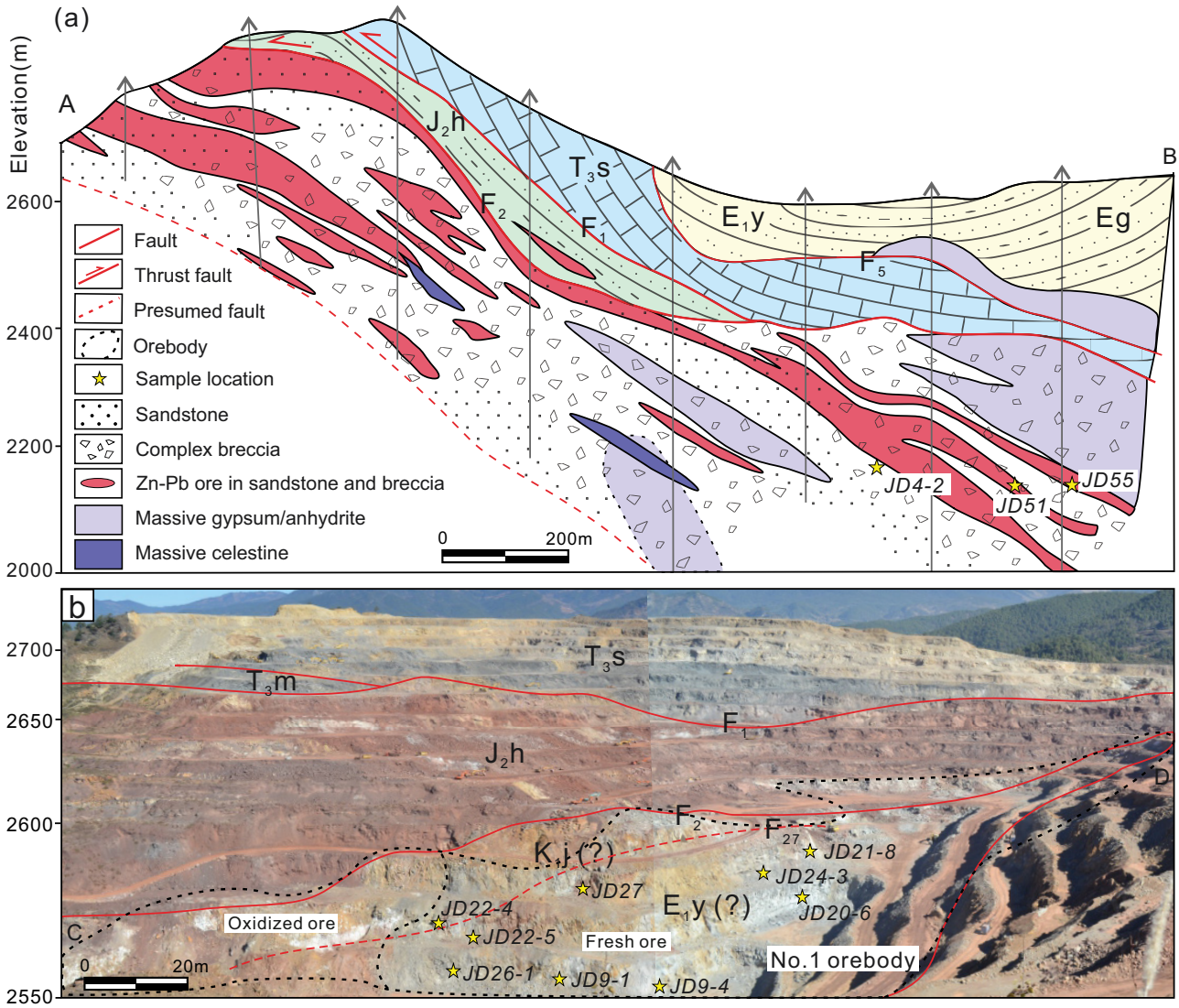

Fig. 2. Geologic section of ore blocks in the Jinding Zn-Pb deposit. (a) Southwest-northeast cross section (A-B section in Fig. 1d) of the Beichang-Paomaping ore block. The Jinding dome is defined by zones of allochthonous succession and complex breccia and sandstone (modified after Tang et al., 2014; Leach et al., 2017). (b) Southeast-northwest section (C-D section in Fig. 1d) of the Beichang open pit with the sampling locations. Abbreviations as in Figure 1d.

from 35.9 to 25.8 Ma or from 26 to 20 Ma, respectively. Based on the spatial relationships between mineralization and regional overthrusting, the earlier timing seems more likely with a proposed window between 33 and 28 Ma (Wang et al., 2009).

More than 100 orebodies have been discovered in the Jinding area. The orebodies are grouped into seven ore blocks: Beichang and Paomaping in the north, Fengzishan and Xipo in the west, Nanchang and Baicaoping in the south, and Jiayashan in the east (Fig. 1c). Orebodies occur as irregular lenses and veins (Fig. 2). The No. 1 orebody in the Beichang block is up to 54 m thick and 1,450 m in length, with a downward extension exceeding 1,000 m in some places. This orebody accounts for ~75% of the total ore reserves in the deposit (Fig. 2; Third Geological Team, 1984; Luo et al., 1994). The host rocks of the orebodies are mainly the sandstones of the Late Cretaceous Jingxing and the Paleocene Yunlong Formations (Third Geological Team, 1984; Gao, 1989; Qin and Zhu, 1991). Recently, Leach et al. (2017) reinterpreted the host-rock sequence as a mixed, sediment-evaporite glacier zone that does not belong to a specific sedimentary formation.

Mineralogy and paragenesis

The major ore types of the Jinding deposit are disseminated, breccia, and vein ores. The disseminated textures mainly occur in the upper part of an individual orebody. They are composed of disseminated sulfides (sphalerite, galena, pyrite, and marcasite) in the matrix of sandstones and limestone clast-bearing sandstones (Fig. 3a, b). In the Beichang ore block, the

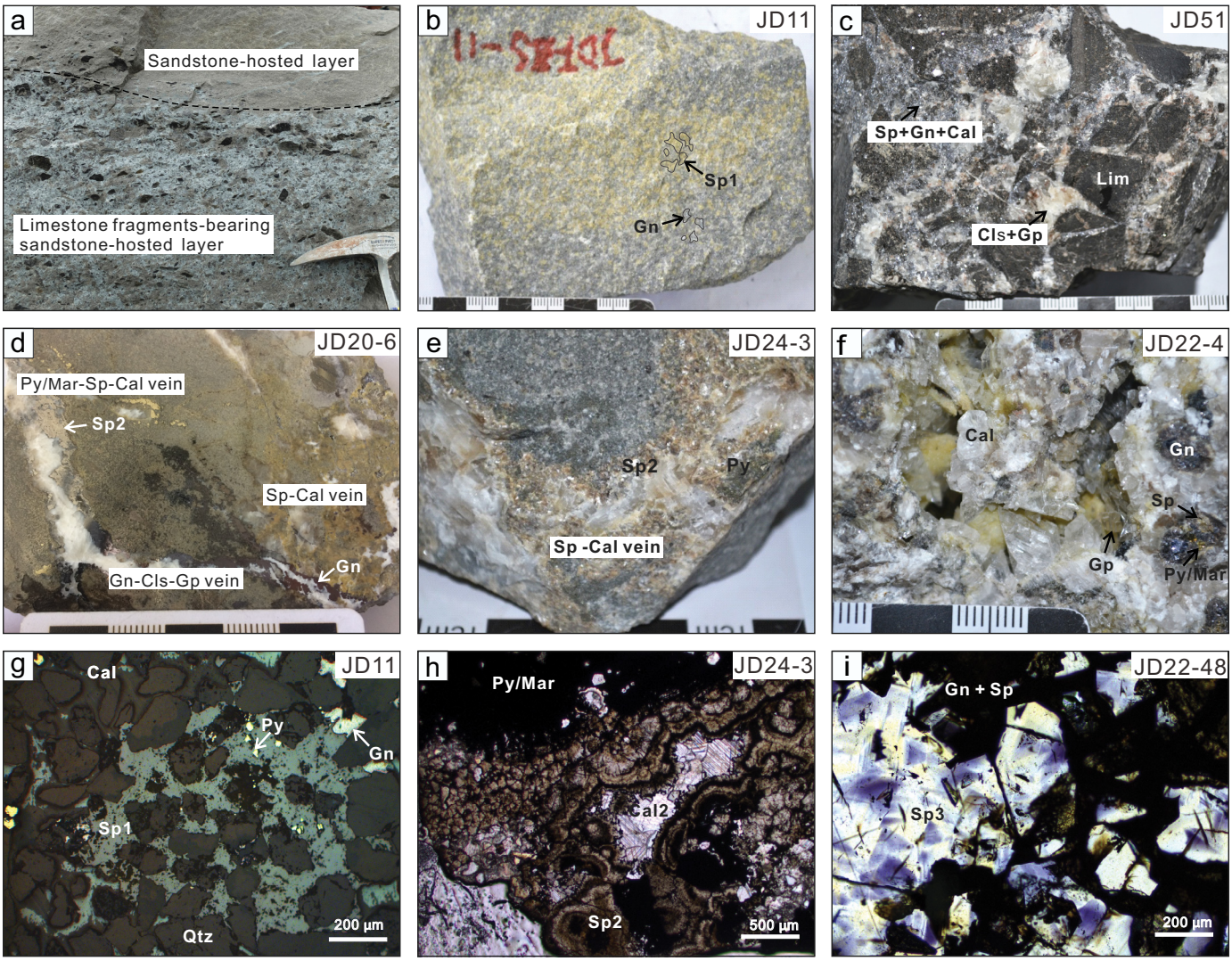

Fig. 3. Hand specimens of typical ores and photomicrographs in transmitted light and reflected light from the Jinding Zn-Pb deposit. (a) Disseminated mineralization in sandstone and limestone-bearing sandstone layers. (b) Disseminated sulfides in sandstone. (c) Angular and chaotic limestone clasts in calcite and gypsum matrix with some galena and minor sphalerite. (d) Sulfide veins in the early disseminated sandstone ore, where the sphalerite-calcite-pyrite/marcasite vein precipitated earlier than the galena-sphalerite-calcite vein. (e) Coarse-grained sphalerite-calcite vein grown along the sandstone. (f) Coarsely crystalline sphalerite, calcite, coarse-grained galena, and minor gypsum filling in cavities. (g) Disseminated sphalerite (Sp1), galena, and pyrite/marcasite replace the carbonate matrix and occur in the interval of quartz clasts in sandstone. (h) Colloform sphalerite (Sp2)-calcite (Cal2) veins intergrown with pyrite and sandstone. (i) Coarsely crystalline sphalerite (Sp3) associated with galena. Cal = calcite, Cls = celestine, Gn = galena, Gp = gypsum, Lim = limestone breccias, Mar = marcasite, Py = pyrite, Qtz = quartz clasts, Sp = sphalerite.

average Zn/Pb ratio of this type of ore is 4.9 (Bai et al., 1985). The breccia ores mainly occur in the lower part of an orebody (Fig. 3c). The breccias comprise limestone, siltstone, and mudstone clasts (millimeters to meters in diameter), possibly derived from the Late Triassic Sanhedong Formation (Gao, 1989). In this type of ore, sulfides act as a cement around the breccia clasts that are themselves rarely mineralized (Fig. 3c). Vein-type ores are spatially controlled by fractures in sandstones and breccias (Fig. 3d, e). Sulfide mineralization is extensively developed in the fault-related veins and near-vein sandstones and breccias.

The ore minerals are mainly sphalerite and galena. They are typically fine-grained (50–200 μm), occurring as anhedral crystals disseminated in sandstones (Figs. 3b, g, 4a). Small amounts of colloform (microcrystalline) sphalerite and pyrite, commonly with concentric zoning structures, are also present (Figs. 3d, e, h, 4b). This type of sulfide in sedimentary rocks elsewhere in the world has been interpreted as forming from supersaturated solutions by rapid crystallization (e.g., Roedder, 1968). Coarse-grained, crystalline sphalerite crystals, associated with coarse-grained galena, pyrite and calcite, are observed in veins (Figs. 3f, i, 4c). The common gangue minerals are pyrite, marcasite, calcite, celestine, barite, gypsum, anhydrite, dolomite, bitumen, hematite, and minor quartz. It should be pointed out that there are amounts of pre-ore gypsum, anhydrite, calcite, celestine, pyrite, and marcasite in the Jinding deposit, but these have been excluded from this study. Organic matter, such as solid bitumen and heavy oil, is common in the orebodies and in the country rocks.

Based on field relationships and microscopic observations of different types of ores, including mineral paragenesis inferred from textures, the Jinding mineralization can be divided into early and late stages (Fig. 5). Both disseminated and colloform sphalerite are interpreted to have precipitated during

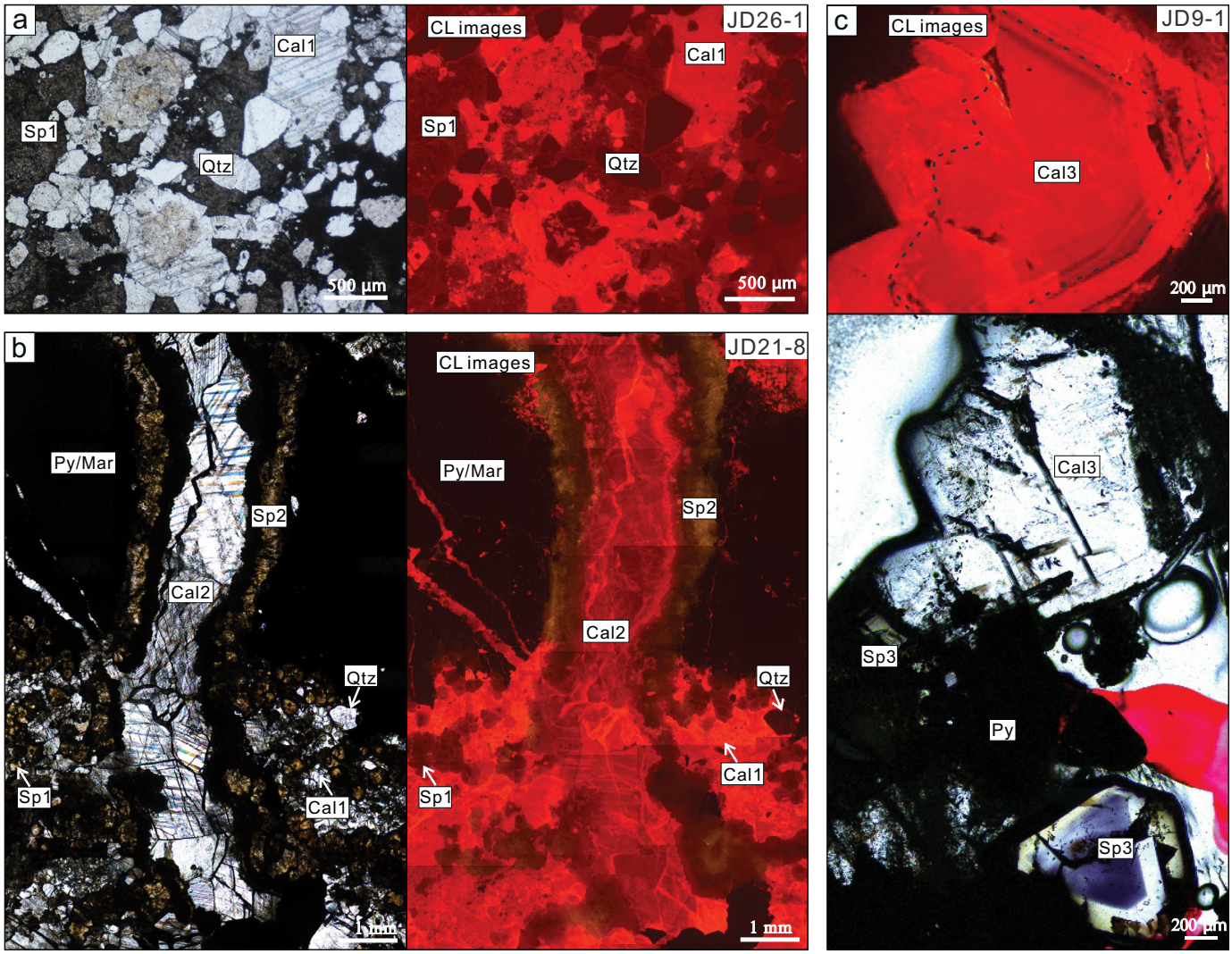

Fig. 4. Photomicrographs in transmitted light and CL images showing characteristics and paragenetic relationships in the different mineralization types of sphalerite at the Jinding deposit. (a) Disseminated sphalerite (Sp1) intergrown with detrital quartz; calcite cement contained a few secondary inclusions. (b) Disseminated sphalerite (Sp1) and fine-grained calcite (Cal1) is crosscut by colloform sphalerite (Sp2)-calcite vein, and coarse calcite (Cal2) has a darker CL color than Cal1. (c) Crystalline sphalerite (Sp3) associated with coarse-grained annular calcite with variable CL colors. Abbreviations are the same as those used in Figure 2.

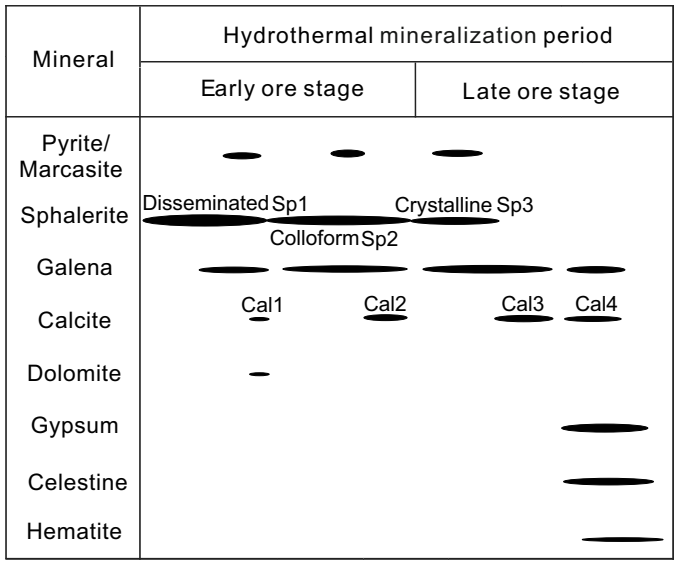

Fig. 5. Paragenetic sequence of hydrothermal minerals in the Jinding deposit.

the early stage. The early-stage disseminated sphalerite (Sp1) commonly occurs as an intergrowth with minor galena, pyrite, and marcasite, cemented by calcite (Cal1, Fig. 3g). The early-stage colloform sphalerite (Sp2) is present in veins with fine-grained calcite (Cal2, Fig. 3e) or with minor amounts of galena and pyrite/marcasite in fractures in sandstones and breccias (Figs. 3h, 4b). Pyrite and marcasite appear to have precipitated relatively early, whereas fine-grained disseminated and colloform sphalerite appear to have precipitated later, as indicated by overgrowth of some colloform sphalerite on pre-ore pyrite and marcasite (Fig. 3h).

The late-stage minerals are generally coarser than the early-stage minerals. The late stage can be further divided into two substages. Coarse-grained galena-calcite veins that crosscut the early-stage sphalerite-calcite veins clearly belong to the late stage, but further classification is not possible (Fig. 3d). Large, euhedral galena and pyrite crystals, translucent euhedral crystalline sphalerite (Sp3), and calcite (Cal3) formed during the earlier substage (Figs. 3f, i, 4c). The calcite crystals in this assemblage are commonly large and euhedral with oscillatory zoning and an annular structure in CL images (Fig. 4c). Large celestine crystals and associated minor amounts of galena and hematite formed during the later substage.

Samples and Analytical Methods

Sample selection

Ore samples were collected from across the Jinding deposit (Fig. 1d). The samples were prepared as doubly polished sections (~200 μm thick) for petrographic observation and fluid inclusion study. A total of more than 200 sections were examined. Thirteen of them contain fluid inclusions that were large enough (>10 μm in diam) for LA-ICP-MS analysis. The selected samples are mainly from the No. 1 orebody in the Beichang block (Fig. 2). Sample descriptions are given in Table 1. The selected samples contain minerals formed at different stages of the mineralization at Jinding, including the colloform and crystalline sphalerites and the fine- to coarse-grained calcite.

Table 1. Locations and Descriptions of the Samples Used for Individual Fluid Inclusion Analyses

Location	Blocks and elevation (m a.s.l.)	Host rock	Mineralogy	Description	Assemblages selected for FI microanalyses	Paragenetic sequence of FI (stage, type)
No. 1 orebody at North Jinding	BC, 2,569	Sandstone	Sp-Gn-Py-Cal	Disseminated sphalerite with bits of galena, pyrite, and marcasite	Cal (JD26-1c)	Early stage, 1
	BC, 2,600	Sandstone	Sp-Gn-Cal	Colloform sphalerite and calcite veins intergrown with disseminated sphalerite	Sp (JD21-8)	Early stage, 2
	BC, 2,580	Sandstone	Sp-Gn-Py-Cal	Colloform sphalerite and calcite veins with bits of pyrite intergrown with sandstone	Sp (JD24-3a), Cal (JD24-3b)	Early stage, 2
	BC, 2,572	Sandstone	Sp-Gn-Py-Cal-Cls	Colloform sphalerite and calcite veins were cut by galena, celestine, and calcite veins	Cal (JD20-6c)	Early stage, 2
	BC, 2,576	Breccias	Sp-Py-Gn-Cal	Crystalline sphalerite intergrown with colloform sphalerite, with bits of galena and pyrite	Sp (JD22-5a), Cal (JD22-5b)	Late stage, 3
	BC, 2,576	Breccias	Sp-Py-Gn-Cal-Gp	Translucent euhedral crystalline sphalerite, pyrite, galena, calcite, and minor gypsum	Sp (JD22-48), Cal (JD22-47)	Late stage, 3
	BC, 2,567	Breccias	Sp-Py-Gn-Cal	Crystalline sphalerite, pyrite, coarse euhedral galena, and zoned calcite	Sp (JD9-1)	Late stage, 3
	BC, 2,567	Breccias	Gn-Sp-Cal	Coarse euhedral galena, translucent euhedral crystalline sphalerite, and pyrite	Sp (JD9-4)	Late stage, 3
	BC, 2,588	Breccias	Cls-Cal-Gn	Coarse celestine and calcite accompanied with galena, intergrown with pre-ore pyrite	Cls (JD27-1, JD27-3)	Late stage, 4
West Jinding	FZS, 2,340	Sandstone	Gn-Sp-Py	Disseminated galena, sphalerite, and locally minor pyrite	NS	
East Jinding	PMP, 2,140	Mainly LBS	Gn-Sp-Gp-Cls-Cal	Coarse celestine and calcite accompanied with galena and locally contained hematite	NS	
	PMP, 2,140	Mainly LBS	Sp-Gn-Py-Hm-Cal	Galena accompanied with celestine and calcite and locally contained hematite	NS	
	PMP, 2,180	Mainly LBS	Gp-Sp	Massive gypsum accompanied with minor sphalerite, and gypsum may be pre-ore	NS	

Abbreviations: a.s.l. = above sea level, BC = Beichang, Cal = calcite, Cls = celestine, FI = fluid inclusion, FZS = Fengzishan, Gn = galena, Gp = gypsum, Hm = hematite, LBS = limestone-bearing sandstone, NS = not successful due to the small size of fluid inclusions, PMP = Paomaping, Py = pyrite, Sp = sphalerite

CL microscopy

Cathodoluminescence microscopy of thin sections was carried out to obtain detailed information on the growth history of the phases hosting the fluid inclusions. A Reliotron luminoscope (type HC1-LM), equipped with a polarization microscope and digital camera, located at the State Key Laboratory of Ore Deposit Geochemistry, Institute of Geochemistry, Chinese Academy of Sciences (IGCAS), was used. The CL images were collected at 5- to 10-kV acceleration voltage and a beam current of 0.5 mA under 80- to 120-mTorr vacuum.

Microthermometry

Microthermometric analysis of fluid inclusions was carried out using a Linkam THMSG600 heating-freezing stage at the State Key Laboratory of Ore Deposit Geochemistry, IGCAS. The temperatures of first melting (Te), final ice-melting (Tm ice), hydrohalite melting (Tm hyd), halite dissolution (Ts NaCl), and homogenization to the liquid phase (Th) were observed and recorded. The measurement precision was ±5°C for Te, ±0.1°C for Tm ice and Tm hyd, and ±1°C for Ts NaCl and Th. The valid ice- and hydrohalite-melting temperatures were used to determine the salinities and weight fractions of NaCl and $CaCl_2$ (i.e., NaCl wt %, $CaCl_2$ wt %, and NaCl/$CaCl_2$) in the NaCl-$CaCl_2$-H_2O system using the numerical model based on empirical best fits of phase equilibria determined from experimental data (Steele-MacInnis et al., 2011, 2016; Schlegel et al., 2012). For the fluid inclusions for which hydrohalite-melting temperatures could not be measured with certainty, the ice-melting temperatures were used to best estimate the salinities.

LA-ICP-MS analysis

The elemental concentrations of individual fluid inclusions were analyzed by LA-ICP-MS at the State Key Laboratory of Ore Deposit Geochemistry, IGCAS, following the procedure described by Lan et al. (2017, 2018). The analytical facility consists of an Agilent 7900 mass spectrometer and a GeolasPro 193-nm ArF excimer laser. Samples were placed into an 8-cm^3 ablation cell and sputtered using a laser with output energy density of 8 J/cm^{-2} and a repetition rate of 6 Hz. The beam size was adjusted to be slightly larger than the fluid inclusions to attain full ablation of the fluid inclusions (e.g, Stoffell et al., 2004), and most sphalerite- and calcite-hosted fluid inclusions were ablated using a laser spot size of 32 μm. Straight ablation methods instead of stepwise ablation were used to drill the target fluid inclusion and yield 80 to 90% successful ablations. NIST SRM-610 was analyzed before and after each batch of 10 inclusions to be used as the external calibration standard and to correct for instrumental drift. Calibration and signal integration of the LA-ICP-MS data were performed using the SILLS program (Guillong et al., 2008).

For data reduction, the internal standards used for correcting host mineral contributions to the ablation signals were Zn for sphalerite and CaO for calcite, based on data acquired by electron probe microanalysis (EPMA) (App. 1). The concentrations of Na were used as an internal standard for determining absolute element concentrations (Gunther et al., 1998; Heinrich et al., 2003). In the sphalerite-hosted fluid inclusions, the method of charge balancing to the NaCl equivalent (Allan et al., 2005) was used to correct for salinity contributions from other chloride salts (e.g., Ca, K, Mg, and Sr) to the freezing point depression-derived estimate. In calcite-hosted fluid inclusions, the determination of Ca concentrations is impossible due to interference from the host calcite, but the salinity has important implications for the LA-ICP-MS data in internal standardization. Therefore, the contents of Ca and Na in calcite-hosted fluid inclusions were estimated using the microthermometric data of valid ice- and hydrohalite-melting temperatures or best estimated NaCl/$CaCl_2$ by numerical models of the NaCl-$CaCl_2$-H_2O system (Steele-MacInnis et al., 2016). An alternative approach of empirical mass balance (Heinrich et al., 1992) is considered to calculate actual compositions here. As a first approximation, the true NaCl content of the fluid can be related to its constituent salts by the empirical relationship and other element concentrations are cast from the analytical ratios (Allan et al., 2005). Fluid inclusions hosted by sphalerite could obtain more reliable Na/Ca values by correcting the total salinity using the charge-balancing method in LA-ICP-MS analyses. Based on the comparison of microthermometric model data and charge balance-calculated LA-ICP-MS data of the sphalerite-hosted fluid inclusions, the composition of Na/Ca in both approaches was approximately consistent with total analytical uncertainties within 15%.

Results

Fluid inclusion petrography

Fluid inclusions for this study were mainly selected from crystalline and colloform sphalerite, oscillatory-zoned calcite, and coarse-grained celestine. The microanalyses mainly focused on FIAs that show evidence for a primary origin and therefore represent the fluid entrapment in each of the paragenetic stages outlined above. Primary fluid inclusions were identified in accordance with the criteria of Roedder (1984) and Goldstein and Reynolds (1994), such as those distributed along growth zones, those occurring as three-dimensional clusters, and those occurring as isolated inclusions. The selected fluid inclusions within concentric growth zones are the best evidence of a primary origin (Fig. 6a, i). Clusters of fluid inclusions and isolated fluid inclusions are possibly primary or secondary, while those fluid inclusions that are away from visible fractures in both sphalerite and calcite in this study are considered to be primary (Fig. 6b-e, j). Trails of fluid inclusions along short, intracrystal healed fractures are considered to be pseudosecondary inclusions (Fig. 6f) and were analyzed for comparison.

At room temperature, three types of fluid inclusions were identified: vapor-liquid biphase fluid inclusions, vapor-liquid-solid triphase fluid inclusions, and organic-rich fluid inclusions. Vapor-liquid fluid inclusions are common in minerals formed at every stage of mineralization. They have irregular, elongated, oval, rectangular, and negative crystal shapes. The sizes range from <5 to 40 μm in diameter, with vapor/liquid ratios from 5 to 8% (Fig. 6a-h). Vapor-liquid-solid triphase fluid inclusions contain a liquid phase, a vapor phase, and a halite crystal (Fig. 6g). The halite-bearing inclusions have never been reported before. This newly found type of fluid inclusions provides direct evidence for the involvement of a high-

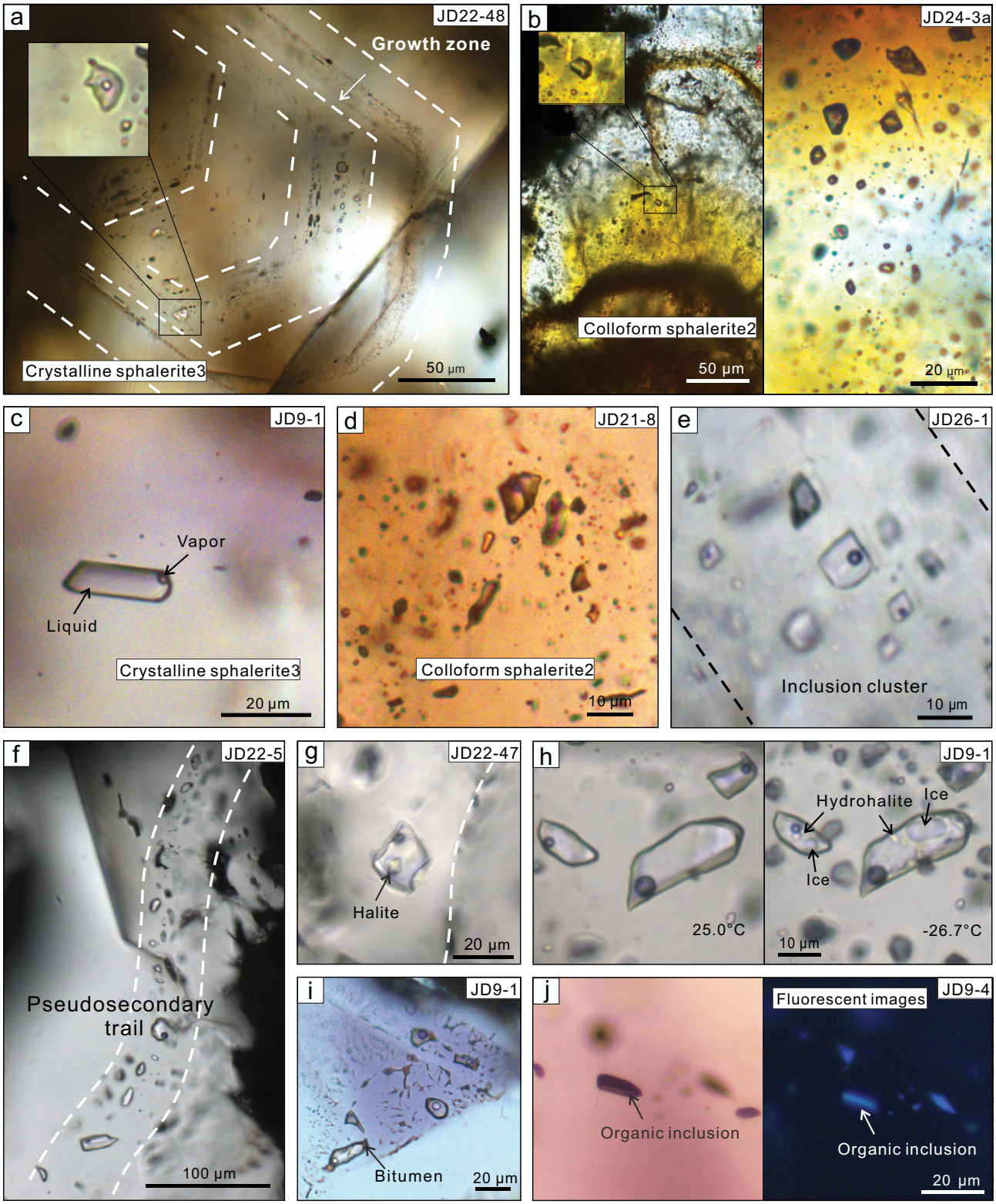

Fig. 6. Representative photomicrographs of different types of fluid inclusions hosted in different minerals. (a) FIAs along growth zones of crystalline sphalerite (Sp3), indicating a primary origin. (b, d) Fluid inclusion clusters in colloform sphalerite (Sp2), indicating a primary origin. (c) Liquid-dominated biphase (liquid + vapor) fluid inclusion cluster in crystalline sphalerite (Sp3). (e) Fluid inclusion cluster in calcite growth zone. (f) An annealed fracture-hosted biphase FIA in calcite, indicating a secondary origin but representing ore fluids. (g) A vapor-liquid halite solid triphase inclusion in calcite. (h) Biphase inclusion at room temperature and at subambient conditions, above the first-melting temperature showing coexisting ice, hydrohalite, solution, and vapor. (i) Biphase organic inclusions and triphase oil inclusions containing solid bitumen in sphalerite. (j) Monophase organic inclusions in sphalerite showing dull blue fluorescence under ultraviolet illumination.

salinity fluid in the formation of the Jinding deposit. Organic-rich fluid inclusions are monophase, biphase, or triphase, with the most prevalent being biphase, irregular, or rounded fluid inclusions containing oil and a vapor phase (Fig. 6i). The oil inclusions under ultraviolet light show whitish yellow to bright-yellow fluorescence colors. Monophase organic gas inclusions show dull-blue fluorescence under ultraviolet light, indicating a composition of low maturity (Fig. 6j). Triphase organic fluid inclusions contain oil, vapor, and solid bitumen (Fig. 6i). The solid bitumen adheres to the wall of the inclusion, possibly because of the precipitation and carbonization of liquid hydrocarbon in a later stage (Roedder, 1984; Lu et al., 2004).

Microthermometry and analysis

The liquid-dominated biphase inclusions were selected for a detailed microthermometric study. The microthermometric data, mainly from FIAs, are summarized in Table 2 (detailed in App. 2). Fluid inclusion data reported in the tables are the FIA averages with 1σ standard deviation.

The aqueous fluid inclusions show no phase change until they are cooled down to temperatures below –50°C. The first-melting temperatures (Tfm) of this type of fluid inclusions occur between –71° and –50°C, indicating that their compositions are at least a NaCl-$CaCl_2$-H_2O ternary system (with a eutectic temperature of –51°C; Roedder, 1984; Goldstein and Reynolds, 1994; Steele-MacInnis et al., 2016). A few fluid inclusions do not freeze completely on cooling or appear to start melting at temperatures as low as –80°C, possibly due to a metastable eutectic (Davis et al., 1990), metastable hydrate crystallization (Samson and Walker, 2000), or perhaps low NaCl/(NaCl + $CaCl_2$) ratios (Chu et al., 2016). Despite this behavior, the melting temperatures of hydrohalite and ice in this type of inclusion can still be used to estimate fluid compositions (Chu et al., 2016). Cyclic cooling and reheating and repeated measurements can be used to make the hydrohalites more observable and to obtain more reliable results (Goldstein and Reynolds, 1994).

Approximately half of fluid inclusions have hydrohalite as the last melting phase. The rest instead have ice as the last melting phase, for which hydrohalite has not appeared or not been observed. A few inclusions have hydrohalite-melting temperatures exceeding the peritectic temperature (0.1°C), as a consequence of metastability or a complex chemical composition, such as the presence of additional salts and CO_2, CH_4, or H_2S in the fluids (e.g., Zwart and Touret, 1994; Gleeson et al., 2000). Ice-melting temperatures in all fluid inclusions were measured and range from –31.8° to –21.6°C for those in sphalerite, from –38.8° to –23.7°C for those in calcite, and from –21.5° to –6.7°C for those in celestine. Pseudosecondary fluid inclusions hosted by Cal1 have relatively low temperature, ranging from –38.8° to –30.2°C. Hydrohalite-melting temperatures that were measured range from –18.7 to –0.2°C for those in sphalerite and from –23.9 to –0.5°C for those in calcite (App. 2).

We have calculated the salinities from the valid ice-melting temperatures and hydrohalite-melting temperatures for the fluid inclusions for which both ice-melting and hydrohalite-melting temperatures were measured. The fluid inclusion compositions plot on the field of hydrohalite (Fig. 7). For the fluid inclusions that have hydrohalite melting above 0.1°C, salinities were calculated using the maximum stable hydrohalite-melting temperature from a given ice-melting temperature using the method described by Rabiei et al. (2017). The salinities of other fluid inclusions with ice as the last melting phase were used as best estimates by the intersecting point of the final ice-melting temperatures and ice-hydrohalite cotectic curve. These results plot on the ice-hydrohalite cotectic boundary of the NaCl-$CaCl_2$-H_2O system, giving the theoretical maximum hydrohalite-melting temperatures and a maximum total salinity, as well as a maximum estimate of NaCl/$CaCl_2$ (Fig. 7; App. 2). The total salinities are almost the same because the isotherms are nearly parallel to the NaCl-$CaCl_2$ tie-line. Therefore, such estimates for sphalerite-hosted fluid inclusions are robust within the uncertainty allowed, as the total salinity is corrected by the charge balance. In fact, the results of LA-ICP-MS indicated that in a given fluid inclusion assemblage, the fluid inclusions with ice or hydrohalite as the last melting phase generally have similar composition. Therefore, we suggest that the composition approximate to the field of hydrohalite (maximum estimate of NaCl/$CaCl_2$) was the best estimate for the calcite-hosted fluid inclusions that lack of hydrohalite-melting temperatures. The range of total salinities (NaCl + $CaCl_2$ equiv) from the sphalerite- and calcite-hosted fluid inclusions are 24.3 to 27.9 and 24.3 to 28.6, respectively (App. 2). The results show that the total salinities of the fluid inclusions are from 10.3 to 29.1 wt %; most of them are between 24.5 and 27.4 wt % with the exception of the Cal1 pseudosecondary fluid inclusions (26.5–28.6 wt %) and Cls4 fluid inclusions (10.3–23.4 wt %). The NaCl/$CaCl_2$ mass ratios, calculated from inclusions where both hydroha-

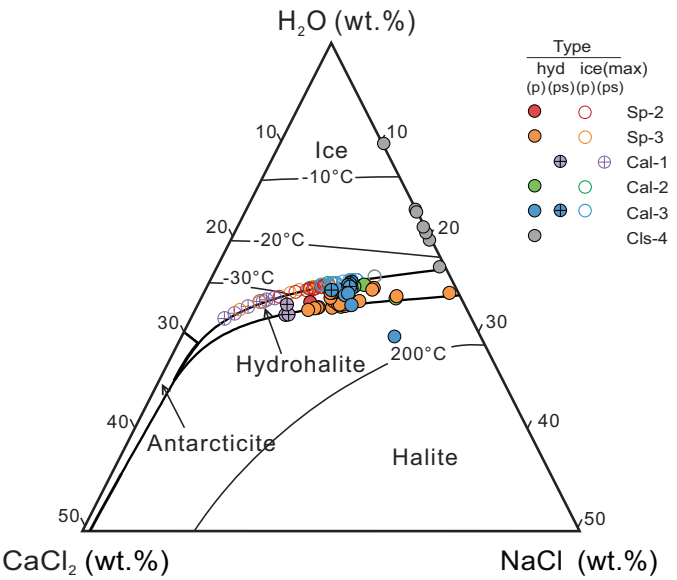

Fig. 7. Ternary H_2O-NaCl-$CaCl_2$ phase diagrams showing the major element composition of fluids in the Jinding deposit. Solid circles represent fluid inclusions with hydrohalite as the last melting phase, and their salinities were calculated from the ice- and hydrohalite-melting temperatures. Hollow circles represent the fluid inclusions with ice as the last melting phase, and their maximum salinities were estimated from the ice-melting temperatures and estimated maximum hydrohalite-melting temperatures. The actual compositions of the fluid inclusions lie above the cotectic curves in the direction of isotherms. The calculation methods and diagrams use the model of Steele-MacInnis et al. (2011). p = primary, ps = pseudosecondary.

Table 2. Microthermometric Data for Analyzed Fluid Inclusion Assemblages from the Jinding Deposit

			Te (°C)		Tm ice (°C)		Tm hyd (°C)		Th (°C)		Ts (°C)	Salinity (wt %)		$NaCl/CaCl_2$		NaCl (wt %)		$CaCl_2$ (wt %)	
FIA ID	Occurrences	Origin	Avg	SD (N)	Avg	SD (N)	Avg	SD (N)	Avg	SD (N)	Avg	Avg	SD (N)	Avg	SD (N)	Avg	SD (N)	Avg	SD (N)
Early-stage type 2 colloform sphalerite																			
JD21-8-3 (1)	Cluster	p	–71	0.5 (2)	–26.5	0.2 (3)	-	-	89	2.7 (3)	-	25.2	0.1 (3)	0.9	0.1 (3)	11.8	0.3 (3)	13.3	0.4 (3)
JD21-8-3 (2)	Cluster	p	–72	2.5 (3)	–27.5	0.6 (4)	–6.7	(1)	103	4.9 (3)	-	26.0	0.8 (4)	0.8	0.2 (4)	11.1	1.5 (4)	14.8	1.0 (4)
JD24-3a (2)	Cluster	p	–69	(2)	–27.8	1.4 (3)	-	-	121	7.2 (3)	-	25.6	0.4 (3)	0.7	0.2 (3)	10.3	1.6 (3)	15.2	2.0 (3)
JD24-3a (4)	Cluster	p	–65	6.5 (3)	–27.5	0.7 (3)	–14.9	(1)	90	9.7 (3)	-	25.8	0.8 (3)	0.8	0.1 (3)	11.2	0.6 (3)	14.7	1.0 (3)
Late-stage type 3 crystalline sphalerite																			
JD22-5a (1)	Isolated	p	–56	-	–25.7	-	-	-	135	-	-	24.9	-	1.1	-	13.1	-	11.8	-
JD22-5a (2)	Cluster	p	–73	0.5 (2)	–22.7	1.1 (3)	–2.8	(1)	165	5.2 (3)	-	25.0	0.8 (3)	1.8	0.4 (2)	15.6	1.0 (2)	8.8	1.2 (2)
JD22-48 (1)	Isolated	p	–70	-	–26.5	-	–0.2	-	140	-	-	27.4	-	1.2	-	14.9	-	12.5	-
JD22-48 (2)	Isolated	p	–70	-	–28.8	-	-	-	129	-	-	25.9	-	0.5	-	9.1	-	16.8	-
JD22-48 (3)	Isolated	p	–71	-	–26.6	-	-	-	104	-	-	25.2	-	0.9	-	11.712	-	13.5	-
JD22-48 (5)	Isolated	p	–72	-	–27	-	–6.8	-	102	-	-	27.1	-	1.0	-	13.7	-	13.4	-
JD22-48 (6)	Isolated	p	–55	-	–24.3	-	–16.3	-	110	-	-	25.5	-	2.0	-	16.8	-	8.6	-
JD22-48 (7)	Isolated	p	-	-	–28	-	-	-	115	-	-	25.6	-	0.6	-	9.9	-	15.7	-
JD22-48 (9)	Growth zone	p	–72	1.6 (3)	–27.1	1.5 (6)	–5.4	1.9 (2)	108	11.5 (6)	-	26.0	1.2 (6)	0.9	0.1 (6)	11.9	0.3 (6)	14.0	1.0 (6)
JD9-1-2 (1)	Cluster	p	–65	(2)	–29	2.6 (2)	-	-	96	2.6 (2)	-	26.0	0.8 (2)	0.6	0.3 (2)	9.1	2.5 (2)	16.9	3.3 (2)
JD9-1-2 (2)	Cluster	p	–68	(1)	–26.9	0.4 (2)	-	-	126	7.3 (2)	-	25.3	0.1 (2)	0.8	0.1 (2)	11.3	0.5 (2)	14.0	0.7 (2)
JD9-4 (1)	Cluster	p	–68	3.2 (9)	–27	0.9 (12)	–3.4	3.1 (8)	117	7.8 (12)	-	26.6	1.1 (12)	1.0	0.2 (12)	13.1	1.3 (12)	13.6	1.2 (12)
JD9-4 (5)	Cluster	p	–69	1.7 (5)	–25.9	1.2 (8)	–12.8	5.6 (6)	114	6.8 (8)	-	26.0	0.5 (8)	1.4	0.6 (8)	14.3	2.7 (8)	11.7	2.4 (8)
Early-stage type 1 fine-grained calcite (intergrown with disseminated sphalerite)																			
JD26-1c (2)	Cluster	ps	–66	1.0 (2)	–36.5	1.9 (3)	-	-	79	2.9 (3)	-	28.0	0.5 (3)	0.2	0.1 (3)	4.3	0.7 (3)	23.7	1.2 (3)
JD26-1c (3)	Cluster	ps	-	-	–32.2	0.2 (2)	-	-	81	0.5 (2)	-	26.9	0.1 (2)	0.3	0.1 (2)	6.3	0.1 (2)	20.5	0.2 (2)
JD26-1c (5)	Cluster	ps	–70	(1)	–31.5	0.1 (3)	–1.4	0.9 (2)	81	2.5 (3)	-	27.9	0.9 (3)	0.4	0.1 (3)	8.8	1.5 (3)	19.1	0.6 (3)
JD26-1c (7)	Cluster	ps	–66	4 (2)	–30.5	0.3 (2)	–17.8	(1)	87	8.3 (2)	-	26.8	0.4 (2)	0.5	0.1 (2)	8.3	0.9 (2)	18.6	0.6 (2)
Early-stage type 2 fine-grained calcite (intergrown with colloform sphalerite)																			
JD20-6c (1)	Growth zone	p	–62	5.4 (3)	–26.4	0.4 (6)	–1.4	0.8 (3)	109	14.2 (5)	-	26.2	1 (6)	1.1	0.2 (6)	13.3	1.7 (6)	12.9	0.9 (6)
JD20-6c (2)	Isolated	p	–59	-	–25.8	-	–5.5	-	114	-	-	26.9	-	1.4	-	15.5	-	11.4	-
JD24-3b (2)	Cluster	p	–57	0.5 (2)	–25	0.3 (3)	–19.9	0.7 (3)	123	0.7 (3)	-	25.3	0.1 (3)	1.5	0.1 (3)	15.1	0.5 (3)	10.2	0.6 (3)
JD24-3b (3)	Isolated	p	–59	-	–25.3	-	–20	-	120	-	-	25.4	-	1.3	-	14.5	-	10.9	-
JD24-3b (5)	Isolated	p	–61	-	–23.7	-	–2.5	-	118	-	-	26.7	-	2.8	-	19.6	-	6.9	-
Late-stage type 3 coarse, crystalline calcite (intergrown with crystalline sphalerite)																			
JD22-5b (3)	Cluster	p	–61	0.8 (3)	–26.4	0.3 (3)	-	-	135	10 (3)	-	25.1	0.1 (3)	0.9	0.1 (3)	12.1	0.4 (3)	13.0	0.8 (3)
JD22-5b (4)	Healed fracture	ps	–58	2.1 (3)	–25.3	0.4 (6)	–21.6	1.6 (6)	127	6.6 (6)	-	25.3	0.3 (6)	1.3	0.1 (6)	14.2	0.7 (6)	11.0	0.8 (6)
JD22-47 (1)	Cluster	p	–59	1.5 (2)	–24.7	0.6 (4)	-	-	108	1.2 (4)	-	24.6	0.2 (4)	1.6	0.4 (4)	14.8	1.1 (4)	9.7	1.3 (4)
JD22-47 (3)	Cluster	p	–61	3.5 (2)	–24.8	0.1 (3)	-	-	123	3.7 (3)	134.2	26.1	2.1 (3)	1.5	0.1 (3)	14.6	0.3 (3)	10.0	0.3 (3)
JD22-47 (4)	Cluster	p	–60	2.1 (3)	–25.9	0.2 (8)	–10.1	6.5 (3)	109	6.3 (8)	-	25.5	0.8 (6)	1.1	0.1 (6)	13.6	1.2 (6)	12.0	0.5 (6)
Late-stage type 4 coarse celestine (intergrown with coarse galena)																			
JD27-1 (1)	Cluster	p	–52	(1)	–7.7	1.0 (2)	-	-	150	2.3 (2)	-	11.5	1.2 (2)	-	-	11.5	1.2 (2)	-	-
JD27-1 (2)	Cluster	p	–60	0.5 (2)	–17.6	0.5 (3)	-	-	144	10 (2)	-	20.6	0.4 (3)	-	-	20.6	0.4 (3)	-	-
JD27-1 (3)	Isolated	p	-	-	–21.5	-	-	-	194	-	-	23.4	-	-	-	23.4	-	-	-
JD27-1 (4)	Isolated	p	-	-	–16.7	-	-	-	-	-	-	19.9	-	-	-	19.9	-	-	-
JD27-1 (6)	Isolated	p	-	-	–14	-	-	-	155	-	-	17.7	-	-	-	17.7	-	-	-
JD27-1 (8)	Isolated	p	–54	-	–16	-	-	-	121	-	-	19.3	-	-	-	19.3	-	-	-
JD27-3 (2)	Cluster	p	–59	5.5 (2)	–14.3	1.9 (5)	-	-	165	8 (5)	-	17.0	1.5 (5)	-	-	17	1.5 (5)	-	-
Oil inclusion in sphalerite 3																			
JD22-48	Cluster	p	-	-	-	-	-	-	104	3.8 (4)	-	-	-	-	-	-	-	-	-
JDBC9-4	Cluster	p	-	-	-	-	-	-	99	5.2 (8)	-	-	-	-	-	-	-	-	-
JDBC9-1-2	Cluster	p	-	-	-	-	-	-	116	4.5 (5)	-	-	-	-	-	-	-	-	-

Notes: - = not determined in the analysis or not quantifiable, FIA = fluid inclusion assemblage, N = number of analyses, p = primary, ps = pseudosecondary, SD = 1 standard deviation, s = secondary

lite melting and ice melting were measured, are mostly from 0.7 to 1.9, although these probably extend to lower values for the inclusions in which hydrohalite melted first but where this was not measured.

The homogenization temperatures of the sphalerite-hosted biphase fluid inclusions range from 79° to 173°C, with a peak between 100° and 130°C (Fig. 8a). The calcite-hosted fluid inclusions mostly have homogenization temperatures between 74° and 144°C, with a peak between 100° and 130°C (Fig. 8b), similar to that of the sphalerite-hosted fluid inclusions. The late-stage fluid inclusions trapped in crystalline sphalerite (Sp3, 118 ± 18°C) and calcite (Cal3, 119 ± 12°C) have higher homogenization temperatures comparable to those hosted by colloform sphalerite (Sp2, 101 ± 15°C) and fine-grained calcite (Cal1, 81 ± 3°C; Cal2, 115 ± 12°C). In contrast, the celestine-hosted fluid inclusions have slightly higher homogenization temperatures overall, varying between 121° and 194°C. The liquid-vapor homogenization temperatures of the organic-rich fluid inclusions in sphalerite are from 88° to 124°C (Fig. 8c). These homogenization temperatures are similar to previously reported data (Xue et al., 2007; Tang et al., 2011; Chi et al., 2017). Higher homogenization temperatures of fluid inclusions trapped in celestine (Xue et al., 2007; Tang et al., 2011) and reported in this study could be due to plastic stretching or partial leakage of inclusions in this soft mineral (Ulrich and Bodnar, 1988) and are therefore considered unreliable. The deformation of host minerals during heating is rare for sphalerite (Wilkinson, 2010). For this reason, we regard the homogenization temperatures of fluid inclusions hosted in sphalerite to be more reliable than those in either calcite or celestite.

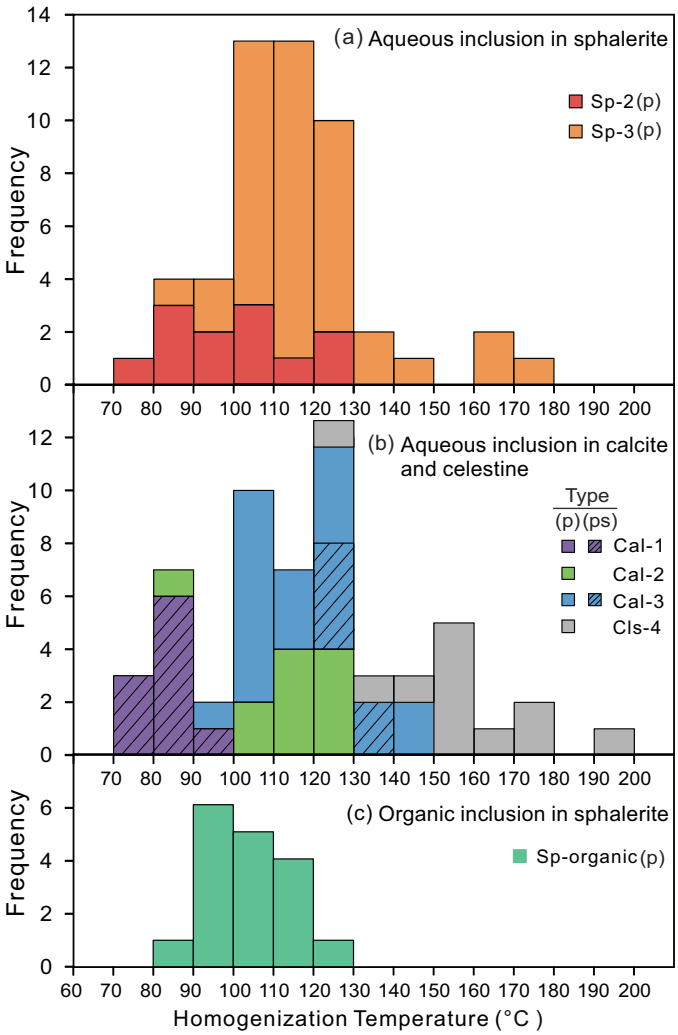

Fig. 8. Histograms of homogenization temperatures of fluid inclusions. (a) Aqueous inclusions in sphalerite. (b) Aqueous inclusions in calcite and celestine. (c) Organic inclusions in sphalerite. p = primary, ps = pseudosecondary.

LA-ICP-MS results

The elemental concentrations of individual fluid inclusions hosted in sphalerite and calcite, determined in situ by LA-ICP-MS, are given in Table 3 and Appendix 3. Our analyses yielded good results for 82 individual fluid inclusions. The elements analyzed include Li, Na, Mg, K, Ca, Mn, Cu, Zn, Rb, Sr, Ag, Cd, Sb, Cs, Ba, Tl, and Pb. The concentrations of most of these elements in both sphalerite- and calcite-hosted fluid inclusions are higher than the detection limits. Ablation of a fluid inclusion in the target is indicated by a sudden increase in Na counts, so the peak of Na during ablation is used to confirm the likelihood that other elements detected were present in the fluid phase (Fig. 9a-c). The good correlations between the intensity for Na (only present in the fluid inclusion) and elements such as Li, Mg, K, Ca, Zn, Rb, Sr, Ag, Sb, Cs, Ba, Tl, and Pb through integration intervals confirm that these elements are predominantly in the fluid phase (e.g., Fig. 9d). The correlations between Na and Cu are flat, and the signals of Cu can be easily overwhelmed by the host mineral contribution even if they may be present in the fluid, so the absolute values were treated with some caution. Analytical artifacts due to the presence of accidental mineral inclusions in a targeted fluid inclusion were eliminated by rejecting analyses where the peak concentration of an element was not correlated with the Na peak. We have also excluded results for elements that have high concentrations in the host minerals, such as Zn, Cd, and Fe in sphalerite and Ca, Mn, and Fe in calcite, from our final data because the host mineral correction is very imprecise in these cases. The concentrations of Ca in the calcite-hosted fluid inclusions were estimated from the microthermometric data instead.

Concentrations of alkali and alkali earth metals generally have a relatively uniform order of magnitude in fluid inclusions of sphalerite and calcite in the Jinding deposit, although calcite-hosted fluid inclusions have a relatively larger variation range for some elements such as Na, Mg, K, Ca, Sr, and Ba (Fig. 10). Pseudosecondary fluid inclusions that are hosted by Cal1 show low content because of the low estimated NaCl/$CaCl_2$ mass ratios, which should be treated with caution for their absolute concentration and focus on their element/Na ratios instead. The abundances of the alkali and alkali earth metals in both sphalerite and calcite-hosted fluid inclusions follow the trend of Na ≥ Ca > Mg > Sr ≥ K > Ba > Li > Rb > Cs, and the Na and Ca contents show the highest average values in both sphalerite-hosted fluid inclusions (49,000 ± 6,000 and 41,000 ± 5,000 ppm, respectively) and calcite-hosted fluid inclusions (49,000 ± 13,000 and 48,000 ± 15,000 ppm, respectively) relative to other elements. The Mg, Sr, and K contents are comparable in magnitude in sphalerite-hosted inclusions

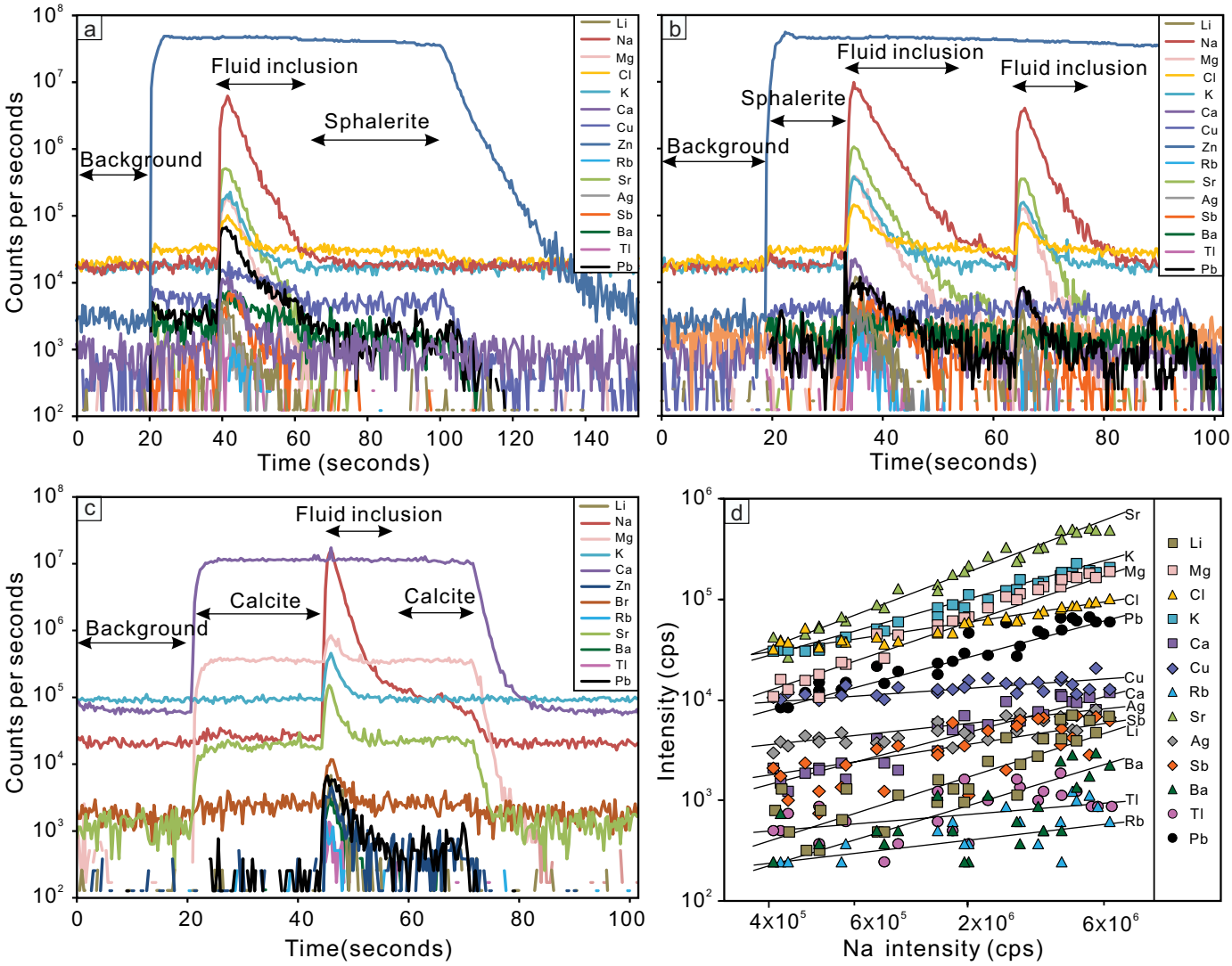

Fig. 9. Transient signal responses for selected elements obtained from LA-ICP-MS analysis. (a, b) Sphalerite-hosted fluid inclusions. (c) Calcite-hosted fluid inclusions. The laser was turned on after approximately 20 s, as indicated by the rapid increase in the Ca and Zn signals. The abrupt increase in the Na signal indicates the beginning of ablation of the target inclusion. (d) The correlations between the intensity for Na (only present in the fluid inclusion) and all elements measured through the integration interval from inclusion (a) confirms their predominance in the fluid phase.

with concentrations of 2,100 ± 600, 1,900 ± 300, and 1,600 ± 500 ppm, respectively. Fluid inclusions in calcite have an average K content of 1,400 ± 400 ppm, which is similar to that in sphalerite, whereas Mg and Sr exhibit wider variations of 3,800 ± 2,000 and 2,100 ± 1,300 ppm, perhaps partly because of imperfect host mineral subtraction. The concentrations of Ba, Li, Rb, and Cs in colloform sphalerite-hosted fluid inclusions (55 ± 19, 27 ± 8, 5 ± 2, and 1 ± 0.1 ppm, respectively) are slightly lower than those in crystalline sphalerite (72 ± 26, 38 ± 14, 5 ± 2, and 1 ± 0.5 ppm, respectively), and fine-grained calcite-hosted inclusions contain the lowest concentrations of these elements (Fig. 10; App. 3).

Compared with alkali and alkali earth metals, metals and semimetals show wider concentration ranges in both sphalerite- and calcite-hosted fluid inclusions and display a striking contrast between the two minerals. As shown in Figure 10, metal concentrations in sphalerite-hosted fluid inclusions are significantly higher by one or two orders of magnitude than fluid inclusions in calcite. As described above, these differences are not due to analytical artifacts. Zinc, Pb, and Tl are detectable in almost all fluid inclusions (Zn is not reported for the sphalerite-hosted fluid inclusions). The average concentrations of Pb and Tl in sphalerite-hosted fluid inclusions are 510 ± 510 and 14 ± 12 ppm, respectively. However, the average Zn, Pb, and Tl concentrations in calcite-hosted fluid inclusions are 98 ± 51, 26 ± 12, and 3 ± 1 ppm, respectively. Other metals, such as Sb, and Ag, are quantified in most of the sphalerite-hosted fluid inclusions, with average concentrations of 61 ± 65 and 79 ± 135 ppm, respectively, also much higher than the calcite-hosted fluid inclusions, which yield average concentrations of 2 ± 1 and 3 ± 1 ppm, respectively (App. 3). It should be noted that given the presence of Pb, Sb, and Ba in the host sphalerite (Fig. 9a, b), the absolute values reported should be treated with some caution.

Table 3. Average Elemental Concentrations (ppm) of LA-ICP-MS Analyses on Each Fluid Inclusion Assemblage in Sphalerite and Calcite from the Jinding Deposit

Sample ID	Inclusion no.	N	Li	Na*	Na	Mg	K	Ca*	Ca	Mn
Type 2 colloform sphalerite										
JD21-8-3	1-1	3	3.3E+1	NU	4.7E+4	2.3E+3	1.6E+3	NU	4.2E+4	2.2E+2
JD21-8-3	2-2	1	3.8E+1	NU	5.6E+4	2.1E+3	1.7E+3	NU	3.9E+4	1.4E+2
JD24-3a	2-1	3	2.6E+1	NU	3.9E+4	3.2E+3	1.3E+3	NU	4.7E+4	5.3E+2
JD24-3a	4-1	3	1.8E+1	NU	4.1E+4	1.6E+3	1.2E+3	NU	4.8E+4	BDL
Type 3 crystalline sphalerite										
JD22-5a	1-1	1	1.8E+1	NU	5.2E+4	2.4E+3	1.6E+3	NU	3.4E+4	BDL
JD22-5a	2-3	1	3.5E+1	NU	6.1E+4	2.9E+3	1.8E+3	NU	3.4E+4	BDL
JD22-48	1-1	1	3.7E+1	NU	5.8E+4	2.0E+3	1.1E+3	NU	BDL	BDL
JD22-48	3-1	1	4.5E+1	NU	4.8E+4	1.9E+3	2.0E+3	NU	4.8E+4	BDL
JD22-48	5-1	1	5.1E+1	NU	5.1E+4	2.4E+3	1.5E+3	NU	3.5E+4	BDL
JD22-48	6-1	1	7.1E+1	NU	5.7E+4	1.8E+3	1.1E+3	NU	3.3E+4	BDL
JD22-48	7-1	1	2.3E+1	NU	4.1E+4	3.4E+3	1.2E+3	NU	4.5E+4	2.3E+2
JD22-48	9-1	3	3.9E+1	NU	4.6E+4	1.6E+3	1.3E+3	NU	4.1E+4	3.1E+2
JD9-1-2	1-1	1	4.2E+1	NU	4.9E+4	2.5E+3	1.5E+3	NU	4.5E+4	1.6E+2
JD9-1-2	2-1	2	2.5E+1	NU	4.7E+4	1.6E+3	1.6E+3	NU	4.1E+4	1.6E+2
JD9-4	1-1	12	4.0E+1	NU	5.2E+4	2.1E+3	1.7E+3	NU	4.0E+4	2.3E+2
JD9-4	5-1	7	3.5E+1	NU	5.1E+4	1.9E+3	1.8E+3	NU	3.8E+4	1.7E+2
Type 1 fine-grained calcite (intergrown with disseminated sphalerite)										
JD26-1c	2-1	3	9.0E+0	1.7E+4	NU	1.6E+3	4.3E+2	8.6E+4	NU	NU
JD26-1c	3-1	1	1.7E+1	2.4E+4	NU	4.3E+2	1.0E+3	7.5E+4	NU	NU
JD26-1c	5-1	3	3.5E+1	3.5E+4	NU	3.7E+3	1.6E+3	6.9E+4	NU	NU
JD26-1c	7-1	2	2.7E+1	3.2E+4	NU	2.0E+3	9.5E+2	6.7E+4	NU	NU
Type 2 fine-grained calcite (intergrown with colloform sphalerite)										
JD20-6c	1-1	6	3.3E+1	5.3E+4	NU	8.3E+3	1.5E+3	4.6E+4	NU	NU
JD20-6c	2-1	1	4.3E+1	6.2E+4	NU	5.0E+3	2.2E+3	4.1E+4	NU	NU
JD24-3b	2-1	3	4.8E+1	5.9E+4	NU	4.1E+3	1.7E+3	3.7E+4	NU	NU
JD24-3b	3-1	2	5.3E+1	5.7E+4	NU	3.3E+2	1.5E+3	3.9E+4	NU	NU
Type 3 coarse, crystalline calcite (intergrown with crystalline sphalerite)										
JD22-5b	3-1	2	2.7E+1	4.8E+4	NU	1.9E+3	1.7E+3	4.7E+4	NU	NU
JD22-5b	4-3	5	4.0E+1	5.6E+4	NU	4.0E+3	1.6E+3	4.0E+4	NU	NU
JD22-47	1-1	4	3.8E+1	5.8E+4	NU	5.6E+3	1.6E+3	3.5E+4	NU	NU
JD22-47	3-1	3	3.4E+1	5.8E+4	NU	4.4E+3	1.4E+3	3.6E+4	NU	NU
JD22-47	4-1	8	4.1E+1	5.3E+4	NU	3.1E+3	1.5E+3	4.3E+4	NU	NU

Notes: BDL = below the detection limit, N = number, Na* and Ca* are calculated from salinities, NU = not used

Discussion

Fluid sources and global compositional comparison

Homogenization temperatures in Jinding fluid inclusions mostly range from 100° to 130°C with small variations within assemblages and show no evidence for systematic stretching or leakage of inclusions and no systematic relationship to depth in the mine. Numerical modeling indicates that fluid overpressures of 100 bar were developed throughout the Lanping basin underneath the nappe, and the ore may have formed in a shallow environment with low lithostatic pressure based on the study of shallow burial of an oil and gas reservoir (<1.3 km; Chi et al., 2005, 2017). Thus, the homogenization temperature values of the homogeneously entrapped inclusions are considered to be approximately equivalent to the fluid trapping temperatures. Fluid salinity is within a small range (24.5–27.4 wt % NaCl + $CaCl_2$ equiv for most assemblages) and has relatively consistent values in each assemblage. The presence of halite-saturated aqueous fluid inclusions confirms this high salinity in fluids. The microthermometric data reported here suggest that the fluids from which the sphalerite and calcite of the Jinding deposit precipitated are likely to have been low-temperature, high-salinity brines.

The molar Cl/Br ratios of fluid inclusions in calcite and celestine determined previously by crush-leach chemical analysis are from 168 to 384 (Fig. 11; Tang, 2013), which are mostly lower than modern seawater ratios but are all within the range of typical basinal brines (Carpenter et al., 1974). Seawater evaporated past the point of halite precipitation has Cl/Br ratios below 655 (Riley and Chester, 1971; McCaffrey et al., 1987), so this process is a likely cause of the range reported. The slight shift of the molar ratios away from evaporated seawater may suggest the effect of fluid-rock reactions, although the uncertainty in these measurements is difficult to constrain. Considering the result of the halogen ratios and microthermometric data, we propose that the ore fluids of the Jinding deposit acquired salinity from evaporation of seawater, some of which may have passed the point of halite precipitation.

In Figure 12, we compare the Jinding ore fluids determined by LA-ICP-MS with some well-known hydrothermal Pb-Zn deposits elsewhere in the world, such as the North American MVT deposits (Stoffell et al., 2008; Appold and Wenz, 2011; Pelch et al., 2015), salt diapir-related MVT deposits (Bouhlel et al., 2016), Irish-type Zn-Pb deposits (Wilkinson et al., 2009), and Schwarzwald basement-derived Zn-Pb deposits (Fusswinkel et al., 2013), as well as some common saline fluids in the crust defined by Yardley (2005), such as sedimentary, metamorphic, and magmatic fluids. In this framework, K/Na ratios are typically higher in magmatic fluids (~0.1–2) and lower in basinal brines (<0.2). The Jinding fluids have low Cs/Na ratios but relatively high Rb/Na, Li/Na, Ba/Na, Ca/Na, Zn/Na, and Pb/Na ratios compared to the typical MVT depos-

Table 3. (*Cont.*)

Sample ID	Cu	Zn	Rb	Sr	Ag	Sb	Cs	Ba	Tl	Pb
Type 2 colloform sphalerite										
JD21-8-3	1.8E+2	NU	4.3E+0	2.0E+3	4.9E+1	2.9E+1	6.0E-1	5.3E+1	1.0E+1	2.8E+2
JD21-8-3	BDL	NU	5.5E+0	1.8E+3	9.8E+0	6.2E+0	6.6E-1	6.4E+1	3.6E+0	1.1E+2
JD24-3a	BDL	NU	2.0E+0	1.8E+3	9.0E+1	1.4E+1	6.5E-1	5.4E+1	3.1E+1	1.9E+2
JD24-3a	3.2E+2	NU	6.8E+0	1.7E+3	6.0E+1	3.7E+1	BDL	5.4E+1	8.8E+0	2.9E+2
Type 3 crystalline sphalerite										
JD22-5a	BDL	NU	BDL	1.8E+3	1.9E+1	BDL	BDL	4.2E+1	2.1E+1	2.4E+2
JD22-5a	BDL	NU	4.6E+0	2.4E+3	BDL	8.2E+1	BDL	6.0E+1	8.9E+0	6.8E+2
JD22-48	1.2E+3	NU	BDL	1.6E+3	1.5E+2	2.0E+2	BDL	BDL	5.2E+1	2.2E+3
JD22-48	BDL	NU	9.6E+0	1.9E+3	6.4E+1	6.7E+1	BDL	6.6E+1	2.0E+1	6.8E+2
JD22-48	BDL	NU	BDL	2.0E+3	7.9E+2	BDL	BDL	4.6E+1	BDL	1.2E+3
JD22-48	BDL	NU	BDL	1.9E+3	6.9E+1	4.2E+1	BDL	8.1E+1	8.6E+0	6.3E+2
JD22-48	1.4E+2	NU	2.5E+0	1.9E+3	3.2E+1	BDL	3.4E-1	3.6E+1	BDL	BDL
JD22-48	5.4E+2	NU	5.7E+0	1.8E+3	1.2E+2	2.0E+2	BDL	6.6E+1	1.2E+1	1.5E+3
JD9-1-2	BDL	NU	4.0E+0	2.2E+3	5.0E+0	4.7E+1	4.6E-1	7.2E+1	6.7E+0	6.6E+1
JD9-1-2	2.3E+2	NU	5.1E+0	1.6E+3	BDL	4.8E+1	BDL	7.6E+1	3.2E+0	1.0E+2
JD9-4	2.8E+2	NU	5.1E+0	2.0E+3	4.9E+1	4.7E+1	1.2E+0	7.7E+1	1.4E+1	4.7E+2
JD9-4	3.2E+1	NU	4.7E+0	1.9E+3	4.1E+0	4.0E+1	1.2E+0	8.0E+1	6.8E+0	1.7E+2
Type 1 fine-grained calcite (intergrown with disseminated sphalerite)										
JD26-1c	BDL	2.2E+1	1.2E+0	6.7E+2	BDL	BDL	BDL	2.3E+0	1.1E+0	7.1E+0
JD26-1c	BDL	4.9E+1	2.7E+0	1.3E+3	BDL	BDL	2.7E-1	2.9E+1	1.6E+0	1.7E+1
JD26-1c	BDL	8.6E+1	2.8E+0	2.0E+3	BDL	BDL	2.8E-1	3.1E+1	1.5E+0	2.7E+1
JD26-1c	BDL	4.2E+1	2.8E+0	2.0E+3	BDL	BDL	2.4E-1	3.8E+1	1.3E+0	7.1E+0
Type 2 fine-grained calcite (intergrown with colloform sphalerite)										
JD20-6c	BDL	1.5E+2	5.4E+0	1.9E+3	BDL	BDL	BDL	3.5E+1	4.1E+0	3.7E+1
JD20-6c	8.9E+0	2.0E+2	4.8E+0	4.0E+3	2.4E+0	BDL	6.6E-1	4.8E+1	4.5E+0	2.4E+1
JD24-3b	BDL	5.4E+1	4.5E+0	3.0E+3	BDL	BDL	5.8E-1	5.4E+1	2.5E+0	1.8E+1
JD24-3b	BDL	9.0E+1	5.4E+0	2.2E+3	3.6E+0	BDL	BDL	6.9E+1	6.2E+0	2.8E+1
Type 3 coarse, crystalline calcite (intergrown with crystalline sphalerite)										
JD22-5b	BDL	7.7E+1	3.4E+0	1.5E+3	BDL	5.1E-1	4.7E-1	2.6E+1	3.7E+0	3.5E+1
JD22-5b	BDL	7.9E+1	4.3E+0	2.7E+3	BDL	BDL	4.3E-1	4.5E+1	2.2E+0	2.3E+1
JD22-47	9.4E+0	1.4E+2	3.9E+0	1.5E+3	BDL	2.5E+0	7.1E-1	3.3E+1	2.3E+0	3.4E+1
JD22-47	5.7E+0	1.3E+2	3.3E+0	2.7E+3	BDL	BDL	BDL	3.5E+1	2.1E+0	3.1E+1
JD22-47	BDL	1.0E+2	3.5E+0	2.0E+3	BDL	BDL	BDL	4.1E+1	2.5E+0	2.6E+1

its. The ore fluids of the Jinding deposit are most comparable to those of the basinal brines and verge toward the metamorphic brine data sets. The Li/Na, Ba/Na (with the exception of the distinctive high Ba/Na in Irish fluids), Ca/Na, Zn/Na, and Pb/Na ratios of the Jinding ore fluids are notably similar to the Irish fluids and the Schwarzwald basement-derived fluids, as well as metamorphic brines (Fig. 12c-g), which reflect salinity-dependent siliciclastic buffering of fluid composition. Thermodynamic buffering by silicate-carbonate mineral assemblages can cause broad, systematic increases in dissolved alkali and alkali earth metals with increasing salinity, which may also enhance solubilization of metals such as Pb and Zn through chloride complexing (Hanor, 1994). It is possible that relatively higher Li, Ba, Ca, Zn, and Pb contents in the Jinding ore fluids compared to typical basinal brines resulted from the interaction of high-salinity fluids with metalliferous sedimentary and/or basement rocks (crustal source indicated by Pb isotope; Tang et al., 2017), as has been suggested for fluids in the Irish deposits and German Schwartzwald (e.g., Fusswinkel et al., 2013; Wilkinson, 2014).

Origin of high Ca contents in the Jinding ore fluids

The results of microthermometric analysis clearly show that the Jinding ore fluids are predominantly of NaCl-$CaCl_2$-H_2O composition, which is common for many large sediment-hosted hydrothermal ore deposits in the world, including shale- and carbonate-hosted Zn-Pb deposits, basement-hosted Pb-Zn deposits, shale-hosted Cu deposits, and unconformity-related U deposits (e.g., Derome et al., 2007; Wilkinson, 2010; Fusswinkel et al., 2013, 2014; Rabiei et al., 2017), as well as some other Zn-Pb deposits in the the Sanjiang Tethyan metallogenic domain where the Jinding deposit is located (Liu et al., 2013; Zou et al., 2016). The results from LA-ICP-MS analysis of individual inclusions of this study reveal that the Jinding ore fluids tend to have high Ca content (41,000 ± 4,000 ppm; Fig. 10) and higher Ca/Na ratios than typical basinal brines, MVT deposits, the Irish fluids, and the Schwarzwald basement-derived fluids (Figs. 12e, 13a).

Ore-forming brines in MVT and SEDEX deposits have been proposed to originate from $CaCl_2$-rich and $MgSO_4$-poor seawater that contained low sulfate concentrations and allowed the fluid to acquire higher concentrations of base metals (Wilkinson, 2014). For forming the Jinding deposit, the brines must have been generated in the Cretaceous to be Ca-Cl_2-seawater derived (Lowenstein et al., 2003) and expelled sometime later, although the data used by these authors are not from the Neo-Tethys Ocean, which the Jinding deposit was associated with. Thus, there are at least two possible explanations for the high Ca contents in the Jinding ore fluids: addition of Ca to the fluids during fluid evolution or the involvement of older (Cretaceous) seawater-derived brines originally trapped within a precursor basin.

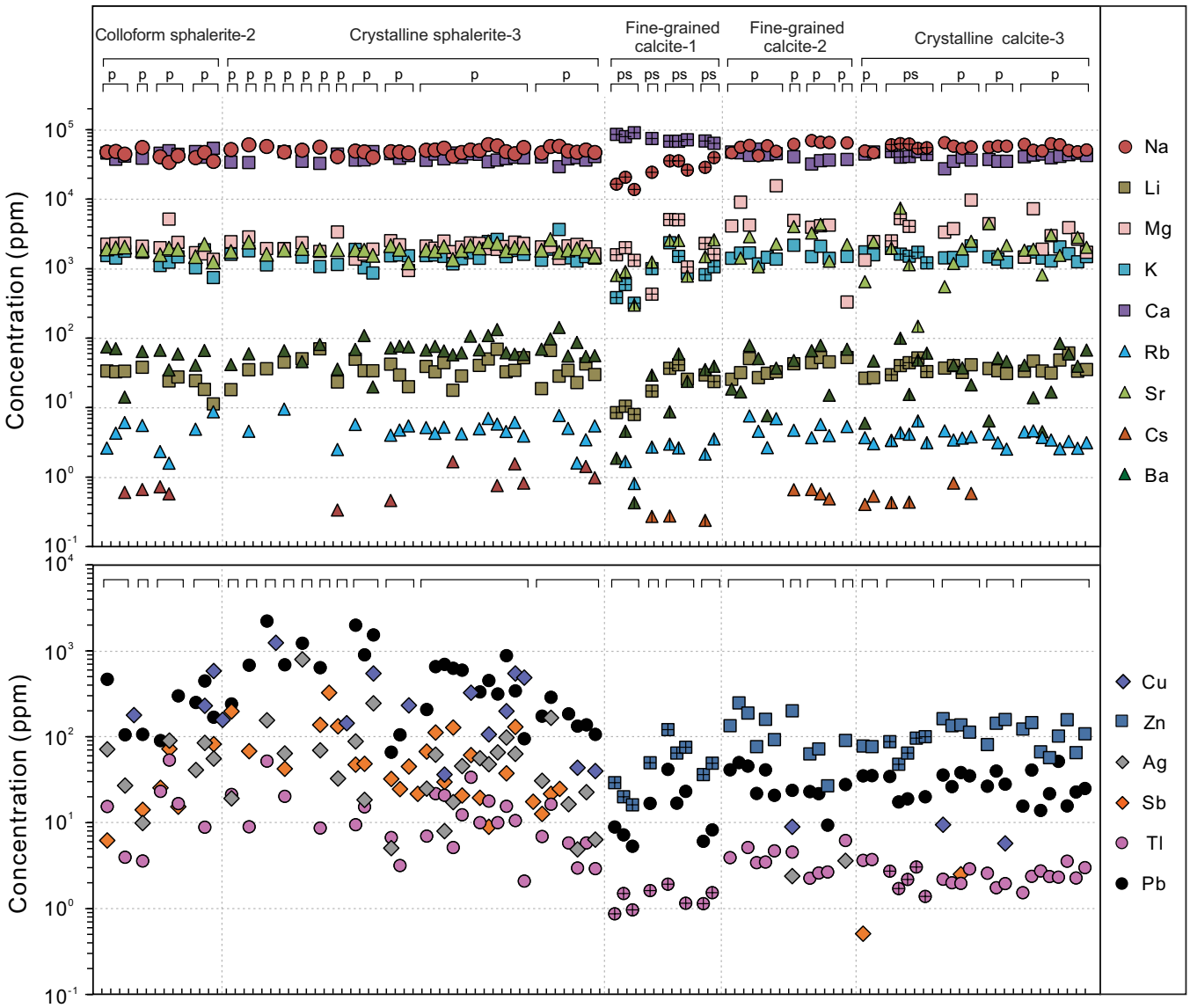

Fig. 10. Summary of chemical composition of fluid inclusion assemblages in sphalerite and calcite determined by LA-ICP-MS microanalysis. Na in both minerals and Ca in calcite were obtained from microthermometry calculations. Zn for sphalerite-hosted fluid inclusions is not displayed because of the interference from the host mineral matrix. p = primary, ps = pseudosecondary.

Fluids may gain calcium from several sources by different processes. Albitization of plagioclase during water-rock interaction is a common process that results in an increase of Ca in the fluid by Ca-Na exchange reactions (Orville, 1972; Baccar et al., 1993; Yardley, 2005). This reaction can proceed in buried sediments or through deep circulation of water in the basement at temperatures as low as 60° to 100°C (Baccar et al., 1993; Davisson et al., 1994; Davisson and Criss, 1996). Carbonate dissolution caused by the precipitation of sulfides from a fluid can also lead to Ca enrichment (Corbella et al., 2004; Williams-Jones et al., 2010). Ca-Mg exchange during dolomitization is another process that can increase Ca in the fluid, but such a process is unlikely to be important for Jinding, because dolomites are rare in the area. Dissolution of gypsum-bearing evaporite is another, and our preferred, explanation for high Ca content in the Jinding ore fluids, as this rock is abundant in the area. The Jinding deposit is hosted by an evaporite dome that was created by the diapiric migration of Late Triassic evaporites (Leach et al., 2017; Song et al., 2020), so the ascending ore fluids have a clear opportunity to acquire Ca from evaporite by dissolution. The composition ratios of Na-Ca-K of the Jinding Cal-1 pseudosecondary fluid inclusions (Fig. 13a) are similar to the saline springs in the Lanping basin, which originated from the Upper Triassic-Paleocene evaporites (Bo et al., 2015). This suggests that they may have similar origin, but the much lower absolute concentrations in saline may be due to an involvement of a large meteoric component (Qi et al., 2018). High Sr contents in the ore fluids support this explanation (Fig. 13b), as Sr-rich minerals such as celestine and gypsum are common in the evaporites at Jinding. Moreover, the explanation is also supported by Sr isotope data. The $^{87}Sr/^{86}Sr$ ratios of gangue minerals in the

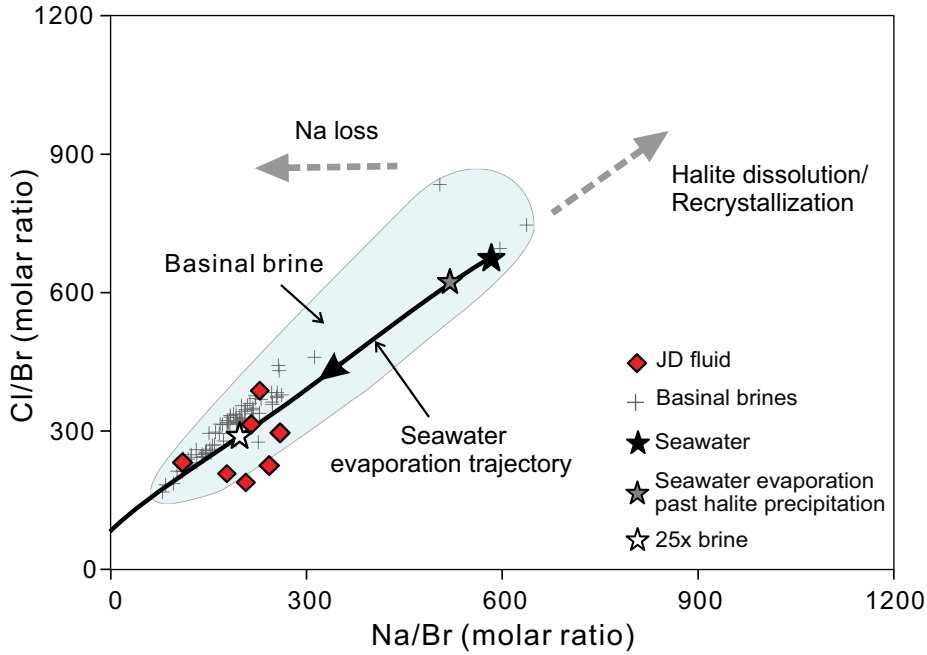

Fig. 11. Na-Cl-Br systematics of measured fluid inclusion compositions from the Jinding deposit. Data from crush-leach analyses of inclusion fluids (Tang, 2013). Seawater evaporation trajectory from McCaffrey et al. (1987). Compositions of modern seawater (Riley and Chester, 1971) and seawater-derived brine with an evaporation ratio of 25× are shown for reference. Basinal brine range from Carpenter et al. (1974).

Jinding deposit are similar to the composition of anhydrites in the region (Tang et al., 2017).

Metals

The LA-ICP-MS data show that there is a population of metal-rich fluid inclusions hosted in sphalerite. LA-ICP-MS traces for Pb and other metals such as Sb, Ag, and Tl show that these elements are clearly present in the fluid phase, confirmed by their good correlations with Na intensity (Fig. 9d). As shown in Figure 10, overall, the FIAs show broadly constant (within approximately half to one order of magnitude) Pb, Sb, Ag, and Tl concentrations, but variations up to one order of magnitude are observed between some FIAs and within a few FIAs despite rigorous data screening. It is possible that such variations resulted from blending of bits of liquid hydrocarbon coexisting with brine inclusions in the sphalerites. Zinc has a strong chemical affinity for carboxylic acids in crude oil (Sanz-Robinson and Williams-Jones, 2019), and some hydrocarbon-bearing fluid inclusions may be enriched in metals compared to coeval brine fluid inclusions (Hurtig et al., 2018).

As shown in Figure 14, Pb and Zn concentrations in most natural fluids are well correlated due to their similar geochemical behavior and buffering by trace sphalerite and galena in the aquifer rocks (Yardley, 2005). We have used this empirical relationship and the measured Pb concentrations to estimate the likely concentrations of Zn in the sphalerite-hosted fluid inclusions following the procedure of Wilkinson et al. (2009). The interquartile range of Pb concentrations in the sphalerite-hosted fluid inclusions is from 200 to 650 ppm. Based on this range, the calculated 25th to 75th percentile Zn concentrations in the fluid inclusions are 200 to 6,500 ppm Zn (Fig. 14), which is comparable to the fluid compositions of many world-class Pb-Zn deposits (e.g., Pb concentrations display 10 to 1,500 ppm in Northern Arkansas sphalerite and 22 to 890 ppm in Ireland, and estimated Zn concentrations up to 3,000 ppm in Northern Arkansas sphalerite and 5,000 ppm in Irish fluids; Stoffell et al., 2008; Wilkinson et al., 2009; Appold and Wenz, 2011). These suggest that the invasion of unusually metalliferous brines is critical for the formation of giant Zn-Pb systems such as Jinding.

By contrast, the Pb and Zn concentrations of the calcite-hosted fluid inclusions at Jinding are relatively low, with interquartile ranges of Pb concentrations from ~10 to ~40 ppm and Zn concentrations from ~20 to ~100 ppm. The different Pb and Zn contents between sphalerite-hosted fluid inclusions and calcite-hosted fluid inclusions may reflect different parental fluid compositions during crystallization of the two host minerals. In other words, the fluid from which sphalerite precipitated was very rich in metals, whereas the fluid from which calcite precipitated was relatively poor in metals. The true reason demands further investigation, but it is clear that such differences are also present in a number of MVT deposits (Fig. 14; Stoffell et al., 2008; Wilkinson et al., 2009; Wenz et al., 2012; Smith-Schmitz and Appold, 2018). Data from the Irish deposits show that the fluid inclusions hosted in the quartz of barren veins are very poor in metals and do not represent the metal compositions of the ore fluids for the associated deposits in the area (Wilkinson et al., 2009). Similarly, the fluid inclusions hosted in the sphalerite and quartz of some MVT deposits in the Tri-State district have different halogen chemistries and are thus considered to have different origins (Stoffell et al., 2008; Wilkinson et al., 2009). In contrast, there are other hydrothermal Pb-Zn deposits in the

world that have high metal concentrations in fluid inclusions hosted in gangue minerals such as quartz and fluorite, which more likely represent the mineralizing fluids instead of independent ones (Fig. 14; Pering Zn-Pb deposit, Huizenga et al., 2005; Schwarzwald basement-derived Zn-Pb deposit, Fusswinkel et al., 2013; Bou Jaber Ba-F-Pb-Zn deposit, Bouhlel et al., 2016).

In the Jinding deposit, alkali and alkali earth metals (e.g., Na, Ca, Mg, Sr, K, Ba, Li, Rb, and Cs) in the fluid inclusions hosted in sphalerite and calcite are rather similar (Fig. 10). The homogenization temperatures and salinities of these two different hosts of fluid inclusions are also similar (Figs. 7, 8). Thus, an alternative model for the difference in metal content could be that the same fluids were involved but that episodes of calcite precipitation occurred at the waning stage of fluid influx once much of the metal had already been precipitated in sulfides.

Ore genesis

Our new data clearly show that the fluids from which sphalerite, the principal ore mineral of the Jinding Pb-Zn deposit, precipitated are enriched in metals relative to most typical crustal fluids. Based on this observation, we suggest that metal-rich brines were probably a prerequisite for the formation of the Jinding deposit specifically, and sediment-hosted Zn-Pb deposits in general. However, this does not rule out the importance of other factors in ore genesis. A recent study of trace occurrences of MVT mineralization by Field et al. (2020) suggested that metal-rich fluids alone cannot produce a giant MVT ore deposit, and the availability of a high concentration of reduced sulfur may also control MVT deposit size. Based on phase equilibria and solubility constraints, simultaneous transportation of abundant metals and sulfides by the ore fluids of these deposits appears unlikely (Stoffell et al., 2008; Appold and Wenz, 2011; Pelch et al., 2015). High Ca and Ba concentrations of up to 50,000, 3,000, and 100 ppm in sphalerite and calcite-hosted fluid inclusions at Jinding indicate that sulfate concentrations in the ore fluids also must have been low because otherwise insoluble sulfates like barite would have precipitated. This raises the question of how the metal-rich brines precipitated sulfides effectively in the time available for mineralization at Jinding. We propose that this resulted from mixing of the brines with another fluid that had low concentrations of metals but high concentrations of reduced sulfur. The paleohydrocarbons trapped in the cap of the Jinding dome could have produced large amounts of reduced sulfur by bacterial reduction and/or thermochemical reduction of sulfates in the associated evaporites, such as gypsum (Tang et al., 2014; Xue et al., 2015; Chi et al., 2017). We suggest that this oil reservoir of aqueous fluid containing abundant reduced sulfur mixed with the highly saline anomalously metalliferous ore fluid, thereby driving sulfide deposition (Fig. 15). It should be pointed out that our data generally support the comparable model of Leach et al. (2017), which articulated that evaporite diapirs in the Jinding dome produced structural traps that provided spaces for accumulation of potential hydrocarbons and reduced sulfur and also for precipitation of metal sulfides when metal-rich brines invaded.

Conclusions

New findings and conclusions from microthermometric and LA-ICP-MS analyses of individual fluid inclusions from the Jinding Zn-Pb deposit are as follows:

1. The Jinding ore fluids are low-temperature (predominantly 100°–130°C), high-salinity (mainly 24.5–27.4 wt %), and Na-Ca–rich (avg $NaCl/CaCl_2$ of 1.3) basinal brines. The presence of halite and high Ca contents in some of the fluid inclusions is a new discovery by this study. We attribute the observed high salinities in the fluid inclusions to evaporation of seawater past the point of halite, which formed the proto-ore fluid bittern brines. The evaporated brines flowed and circulated in metal-fertile sedimentary/basement sequences, and evaporitic sequences resulted in intense fluid-rock interactions that were effective at leaching metals Pb and Zn and elements Li, Ba, and Ca. The compositions of the final ore fluids of the Jinding deposit are similar to basinal brines/basement interacted brines, verging on metamorphic brines.
2. The fluid inclusions hosted in ore and gangue minerals have similar temperatures, salinities, and major elemental compositions but different metal concentrations, with the former containing significantly higher metal concentrations than the latter. We propose that this difference is due to precipitation of the ore minerals prior to calcite in a series of fluid influxes, as represented by the multiple paragenetic stages described. Our new data also show for the first time that the ore fluids of the Jinding deposit contain abundant ore metals (~200–650 ppm Pb and ~200–6,500 ppm Zn) and other metals (~60 ppm Sb, ~80 ppm Ag, and ~15 ppm Tl), comparable with other major sediment-hosted Zn-Pb deposits worldwide. This suggests that involvement of such

Fig. 12. Plots of K/Na mass ratio versus other elemental/Na ratios for FIAs (a-g) from the Jinding deposit and other giant Pb-Zn deposits. Error bars are at 1σ level. Some error bars are smaller than the symbols. Light blue, green, and red fields delimit compositions of saline fluids in sedimentary, metamorphic, and magmatic environments, respectively. The database construction is based on Yardley (2005) and Heijlen et al. (2008) and references therein. Compositions of the North American MVT deposits (Stoffell et al., 2008; Appold and Wenz, 2011; Pelch et al., 2015), salt diapir-related MVT deposits (Bouhlel et al., 2016), Irish-type Zn-Pb deposits (Wilkinson et al., 2009), and Schwarzwald basement-derived Zn-Pb deposits (Fusswinkel et al., 2013) are shown for comparison. Basinal brine field data are from Carpenter et al. (1974), Kharaka et al. (1987), Connolly et al. (1990), Lundegard and Trevena (1990), Stueber and Walter, 1991; Wilson and Long (1993), Fontes and Matray (1993), Morad et al. (1994), Stueber et al. (1998), Kloppmann et al. (2001), Martel et al. (2001), Michael et al. (2003), and Worden et al. (2006). Metamorphic brine field data are from Banks et al. (1991), Munz et al. (1995), Meere and Banks (1997), McCaig et al. (2000), Boiron et al. (2002), Dewaele et al. (2004), Miron et al. (2013), Marsala et al. (2013), and Rauchenstein-Martinek et al. (2016). Magmatic fluid field data are from Heinrich et al. (1992), Campbell et al. (1995), Kamenetsky et al. (2002), Smith et al. (1996), Ulrich et al. (2001), Rusk et al. (2004), Landtwing et al. (2005), Klemm et al. (2007), Samson et al. (2008), Williams-Jones et al. (2010), Shu et al. (2017), and Chang et al. (2018).

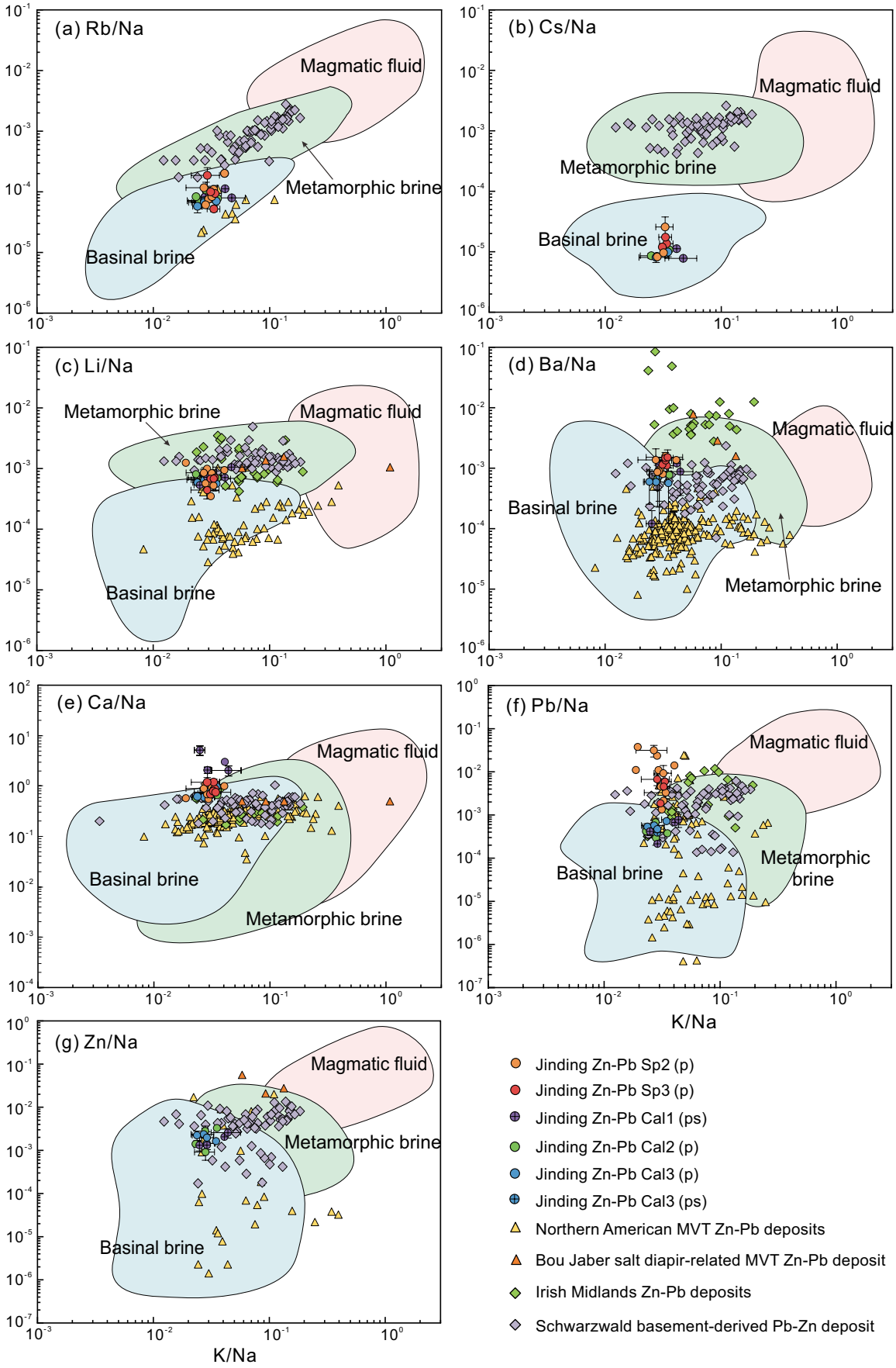

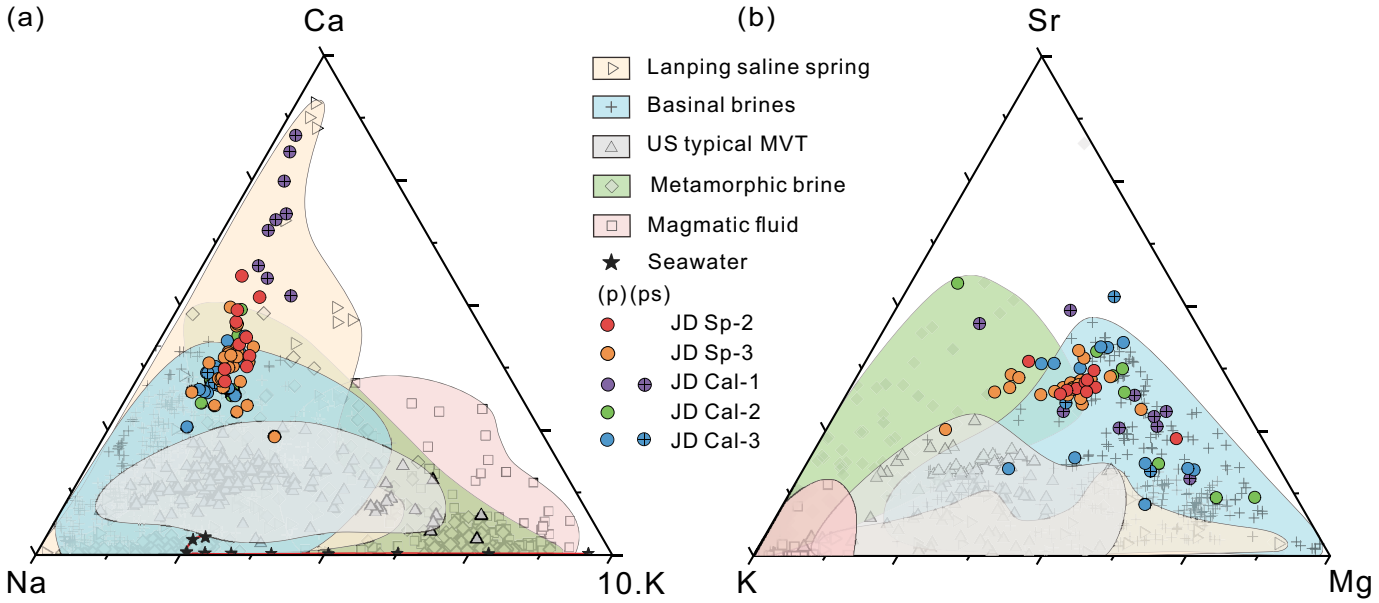

Fig. 13. Comparison of fluid chemistry in Na-Ca-K (a) and K-Mg-Sr (b) diagrams for the Jinding (JD) deposit with the end-member fluid fields for other types of fluid. Sedimentary, metamorphic, and magmatic brine fields are the same as those used in Figure 12. Saline springs in the Lanping-Simao basin are from Bo et al. (2015), Wang et al. (2017) and Qi et al. (2018). p = primary, ps = pseudosecondary.

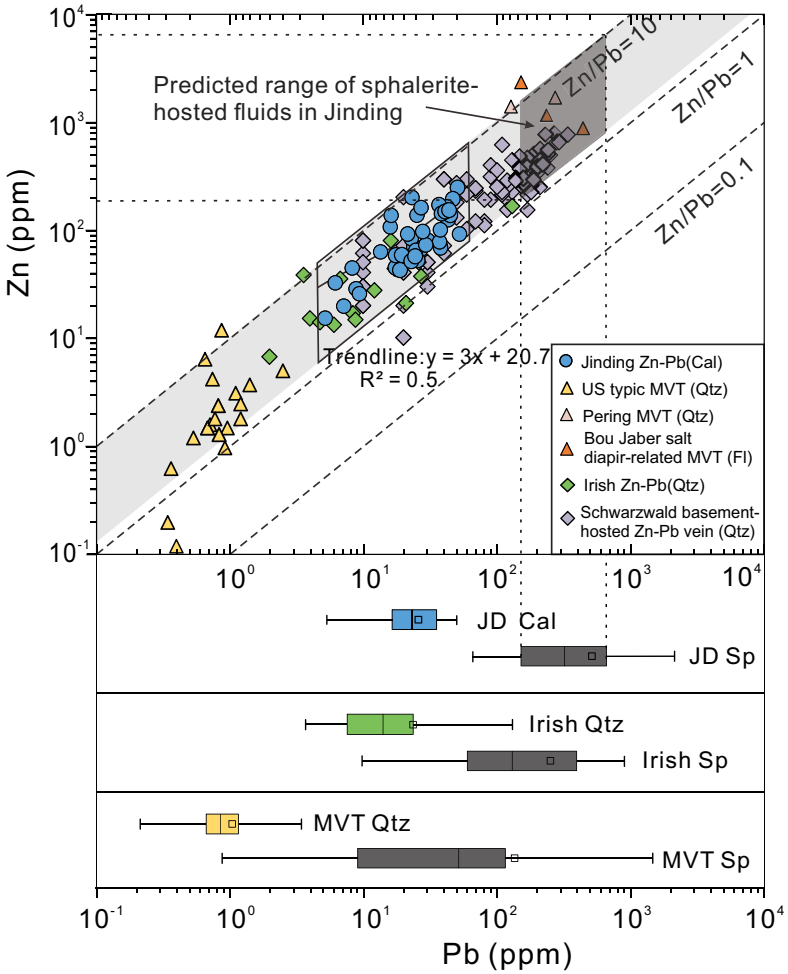

Fig. 14. Correlation plot of Pb and Zn concentrations and comparison of Pb concentration trapped by ore minerals and gangue minerals. The Zn concentration of sphalerite-hosted inclusions in Jinding is predicted based on the extrapolation of the observed empirical correlation of Zn and Pb concentrations in crustal fluids (Wilkinson et al., 2009), as delineated by the gray field. Typical Zn/Pb ratios (by mass) for natural fluids are in the range of 1 to 10 (see dashed lines). Data sources are Huizenga et al. (2005), Stoffell et al. (2008), Wilkinson et al. (2009), Appold and Wenz (2011), Fusswinkel et al. (2013), Pelch et al. (2015), and Bouhlel et al. (2016). Whiskers of box plots represent the maximum and minimum of data, box edges represent 25th and 75th percentiles, inner lines represent medians, and squares represent means. Abbreviations: Cal = calcite, Fl = fluorite, JD = Jinding, Qtz = quartz, Sp = sphalerite.

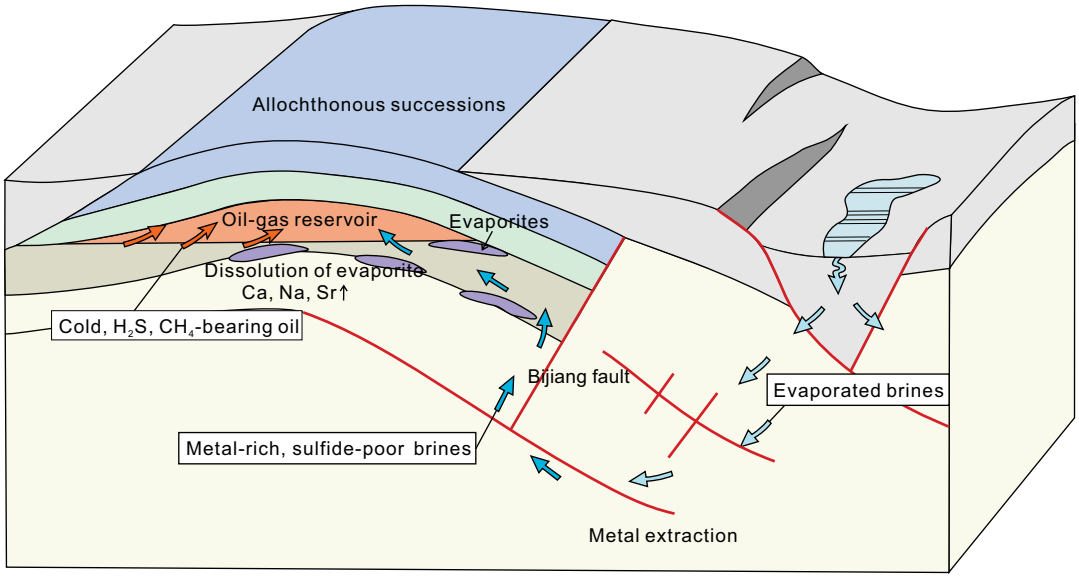

Fig. 15. A schematic cartoon showing fluid processes for the formation of the Jinding deposit. The colored arrows represent the direction of fluid flow, and red lines represent primary fault conduits for fluid flow. The principal ore fluids were produced from evaporated seawater. The evaporated brines flowed and circulated in metal-fertile sedimentary/basement sequences due to the extensive fracture permeability and resulted in intense fluid-rock interactions that were effective at leaching metals such as Pb and Zn. The evaporites in the sequence flowed into and infiltrated thrusts and effectively lubricated tectonic displacements to produce tectonic domes that provided structural traps for hydrocarbons generated during the maturation of organic matter in the rocks (Leach et al., 2017). This oil-gas reservoir was formed in a shallow (<1.3 km) and low-temperature (<80°C) environment (Chi et al., 2017). Metal-rich brines flowed upward along the Bijiang fault and into the dome and mixed with a resident H_2S-bearing oil to form the giant Jinding Pb-Zn deposit.

unusually metal-rich fluids is a prerequisite for the formation of world-class Zn-Pb deposits.

3. We recognize that additional large amounts of reduced sulfur are also required for ore precipitation and that these are unlikely to have been supplied by the metalliferous ore fluids. We propose that ore deposition was achieved by mixing of metal-rich, sulfide-poor ascending brines with a reduced, sulfur-rich fluid that was produced by bacteria-assisted reaction of hydrocarbons with gypsum-bearing evaporites in the cap of the Jinding dome.

Acknowledgments

This research was financially supported by the Strategic Priority Research Program (B) of the Chinese Academy of Sciences (XDB18000000) and the National Science Foundation of China (41830432, 41703047, and 41973047). We thank Profs. Yan Tao and Jiafei Xiao for their help during field work, and Yanwen Tang and Jiali Cai for their assistance in fluid inclusion analysis. We have benefited enormously from discussion with Profs. Chusi Li, David Leach, and Guoxiang Chi. Constructive reviews from Prof. Martin Appold and an anonymous reviewer are greatly appreciated. We are indebted to Associate Editor Dr. Jamie Wilkinson for his detailed guidance for revision as well as for numerous technical corrections and thorough language editing.

REFERENCES

Allan, M.M., Yardley, B.W.D., Forbes, L.J., Shmulovich, K.I., Banks, D.A., and Shepherd, T.J., 2005, Validation of LA-ICP-MS fluid inclusion analysis with synthetic fluid inclusions: American Mineralogist, v. 90, p. 1767–1775.

Appold, M.S., and Wenz, Z.J., 2011, Composition of ore fluid inclusions from the Viburnum trend, southeast Missouri district, United States: Implications for transport and precipitation mechanisms: Economic Geology, v. 106, p. 55–78.

Audetat, A., Gunther, D., and Heinrich, C.A., 1998, Formation of a magmatic-hydrothermal ore deposit: Insights with LA-ICP-MS analysis of fluid inclusions: Science, v. 279, p. 2091–2094.

Audetat, A., Gunther, D., and Heinrich, C.A., 2000, Causes for large-scale metal zonation around mineralized plutons: Fluid inclusion LA-ICP-MS evidence from the Mole granite, Australia: Economic Geology, v. 95, p. 1563–1581.

Baccar, M.B., Fritz, B., and Made, B., 1993, Diagetic albitization of K-feldspar and plagioclase in sandstone reservoirs-thermodynamic and kinetic modeling: Journal of Sedimentary Petrology, v. 63, p. 1100–1109.

Bai, J.F., Wang, C.H., and Na, R.X., 1985, Geological characteristics of the Jinding lead-zinc deposit in Yunnan, with a special discussion on its genesis: Mineral Deposits, v. 4, p. 1–9 (in Chinese with English abs.).

Banks, D.A., Da Vies, G.R., Yardley, B.W.D., McCaig, A.M., and Grant, N.T., 1991, The chemistry of brines from an Alpine thrust system in the Central Pyrenees: An application of fluid inclusion analysis to the study of fluid behaviour in orogenesis: Geochimica et Cosmochimica Acta, v. 55, p. 1021–1030.

Bi, X.W., Tang, Y.Y., Tao, Y., Wang, C.M., Xu, L.L., Qi, H.W., Lan, Q., and Mu, L., 2019, Composite metallogenesis of sedimenthosted Pb-Zn-Ag-Cu base metal deposits in the Sanjiang collisional orogen, SW China, and its deep driving mechanisms: Acta Petrologica Sinica, v. 35, p. 1341–1371 (in Chinese with English abs.).

Bo, Y., Liu, C.L., Zhao, Y.J., and Wang, L.C., 2015, Chemical and isotopic characteristics and origin of spring waters in the Lanping-Simao basin, Yunnan, Southwestern China: Chemie Der Erde-Geochemistry, v. 75, p. 287–300.

Boiron, M.C., Cathelineau, M., Banks, D.A., Buschaert, S., Fourcade, S., Coulibaly, Y., Michelot, J.L., and Boyce, A., 2002, Fluid transfers at a basement/cover interface. Part II. Large-scale introduction of chlorine into the basement by Mesozoic basinal brines: Chemical Geology, v. 192, p. 121–140.

Bouhlel, S., Leach, D.L., Johnson, C.A., Marsh, E., Salmi-Laouar, S., and Banks, D.A., 2016, A salt diapir-related Mississippi Valley-type deposit: The Bou Jaber Pb-Zn-Ba-F deposit, Tunisia: Fluid inclusion and isotope study: Mineralium Deposita, v. 51, p. 749–780.

Campbell, A.R., Banks, D.A., Phillips, R.S., and Yardley, B.W.D., 1995, Geochemistry of Th-U-REE mineralizing magmatic fluids, Capitan Mountains, New Mexico: Economic Geology, v. 90, p. 1271–1287.

Carpenter, A.B., Trout, M.L., and Pickett, E.E., 1974, Preliminary report on the origin and chemical evolution of lead- and zinc-rich oil field brines in central Mississppi: Economic Geology, v. 69, p. 1191–1206.

Chang, J., Li, J.W., and Audetat, A., 2018, Formation and evolution of multistage magmatic-hydrothermal fluids at the Yulong porphyry Cu-Mo deposit, eastern Tibet: Insights from LA-ICP-MS analysis of fluid inclusions: Geochimica et Cosmochimica Acta, v. 232, p. 181–205.

Chen, H.H., Dobson, J., Heller, F., and Hao, J., 1995, Paleomagnetic evidence for clockwise rotation of the Simao region since the Cretaceous: A consequence of India-Asia collision: Earth and Planetary Science Letters, v. 134, p. 203–217.

Chi, G.X., Qing, H.R., Xue, C.J., and Zeng, R., 2005, An overpressured fluid system associated with the giant sandstone-hosted Jinding Zn-Pb deposit, western Yunnan, China: Mineral Deposit Research: Meeting the Global Challenge, Society for Geology Applied to Mineral Deposits (SGA) Biennial Meeting, 8th, Beijing, 2005, v. 1–2, p. 93–96.

Chi, G.X., Qing, H.R., Xue, C.J., and Zeng, R., 2006, Modeling of fluid pressure evolution related to sediment loading and thrust faulting in the Lanping basin: Implications for the formation of the Jinding Zn-Pb deposit, Yunnan, China: Journal of Geochemical Exploration, v. 89, p. 57–60.

Chi, G.X., Xue, C.J., Lai, J.Q., and Qing, H.R., 2007, Sand injection and liquefaction structures in the Jinding Zn-Pb deposit, Yunnan, China: Indicators of an overpressured fluid system and implications for mineralization: Economic Geology, v. 102, p. 739–743.

Chi, G.X., Xue, C.J., Sun, X., Lai, J., Luo, P., Song, H., Li, S., and Zeng, R., 2017, Formation of a giant Zn-Pb deposit from hot brines injecting into a shallow oil-gas reservoir in sandstones, Jinding, southwestern China: Terra Nova, v. 29, p. 312–320.

Chu, H.X., Chi, G.X., and Chou, I.M., 2016, Freezing and melting behaviors of H_2O-NaCl-$CaCl_2$ solutions in fused silica capillaries and glass-sandwiched films: Implications for fluid inclusion studies: Geofluids, v. 16, p. 518–532.

Chung, S.L., Lee, T.Y., Lo, C.H., Wang, P.L., Chen, C.Y., Yem, N.T., Hoa, T.T., and Wu, G.Y., 1997, Intraplate extension prior to continental extrusion along the Ailao Shan Red River shear zone: Geology, v. 25, p. 311–314.

Chung, S.L., Lo, C.H., Lee, T.Y., Zhang, Y.Q., Xie, Y.W., Li, X.H., Wang, K.L., and Wang, P.L., 1998, Diachronous uplift of the Tibetan Plateau starting 40 Myr ago: Nature, v. 394, p. 769–773.

Connolly, C.A., Walter, L.M., Baadsgaard, H., and Longstaffe, F.J., 1990, Origin and evolution of formation water, Alberta basin, western Canada sedimentary basin: Applied Geochemistry, v. 5, p. 375–395.

Corbella, M., Ayora, C., and Cardellach, E., 2004, Hydrothermal mixing, carbonate dissolution and sulfide precipitation in Mississippi Valley-type deposits: Mineralium Deposita, v. 39, p. 344–357.

Davis, D.W., Lowenstein, T.K., and Spencer, R.J., 1990, Melting behavior of fluid inclusions in laboratory-grown halite crystals in the systems NaCl-H_2O, NaCl-KCl-H_2O, NaC-$MgCl_2$-H_2O, and NaCl-$CaCl_2$-H_2O: Geochimica et Cosmochimica Acta, v. 54, p. 591–601.

Davisson, M.L., and Criss, R.E., 1996, Na-Ca-Cl relations in basinal fluids: Geochimica et Cosmochimica Acta, v. 60, p. 2743–2752.

Davisson, M.L., Presser, T.S., and Criss, R.E., 1994, Geochemistry of tectonically expelled fluids from the northern Coast ranges, Rumsey Hills, California, USA: Geochimica et Cosmochimica Acta, v. 58, p. 1687–1699.

Deng, J., Wang, Q.F., Li, G.J., Li, C.S., and Wang, C.M., 2014a, Tethys tectonic evolution and its bearing on the distribution of important mineral deposits in the Sanjiang region, SW China: Gondwana Research, v. 26, p. 419–437.

Deng, J., Wang, Q.F., Li, G.J., and Santosh, M., 2014b, Cenozoic tectonomagmatic and metallogenic processes in the Sanjiang region, southwestern China: Earth-Science Reviews, v. 138, p. 268–299.

Derome, D., Cathelineau, M., Fabre, C., Boiron, M.C., Banks, D., Lhomme, T., and Cuney, M., 2007, Paleo-fluid composition determined from individual fluid inclusions by Raman and LIBS: Application to mid-Proterozoic evaporitic Na-Ca brines (Alligator Rivers uranium field, Northern Territories, Australia): Chemical Geology, v. 237, p. 240–254.

Dewaele, S., Muchez, P.H., and Banks, D.A., 2004, Fluid evolution along multistage composite fault systems at the southern margin of the Lower Palaeozoic Anglo-Brabant fold belt, Belgium: Geofluids, v. 4, p. 341–356.

Dong, F.L., Mo, X.X., Hou, Z.Q., Wang, Y., Bi, X.M., and Zhou, S., 2005, $^{40}Ar/^{39}Ar$ ages of Himalayan alkaline rocks in Lanping basin, Yunnan Province, and their geological implications: Acta Petrologica et Mineralogica, v. 24, p. 103–109 (in Chinese with English abs.).

Dupont-Nivet, G., Lippert, P.C., van Hinsbergen, D.J.J., Meijers, M.J.M., and Kapp, P., 2010, Palaeolatitude and age of the Indo-Asia collision: Palaeomagnetic constraints: Geophysical Journal International, v. 182, p. 1189–1198.

Field, J.D., Appold, M.S., Coveney, R.M., and Bodnar, R.J., 2020, Geochemical characteristics of trace occurrences of Mississippi Valley-type mineralization in the US mid-continent: Implications for deposit growth: Journal of Geochemical Exploration, v. 213, p. 1–23.

Fontes, J.C., and Matray, J.M., 1993, Geochemistry and origin of formation brines from the Paris basin, France: 1. Brines associated with Triassic salts: Chemical Geology, v. 109, p. 149–175.

Fusswinkel, T., Wagner, T., Walle, M., Wenzel, T., Heinrich, C.A., and Markl, G., 2013, Fluid mixing forms basement-hosted Pb-Zn deposits: Insight from metal and halogen geochemistry of individual fluid inclusions: Geology, v. 41, p. 679–682.

Fusswinkel, T., Wagner, T., Wenzel, T., Walle, M., and Lorenz, J., 2014, Red bed and basement sourced fluids recorded in hydrothermal Mn-Fe-As veins, Sailauf (Germany): A LA-ICPMS fluid inclusion study: Chemical Geology, v. 363, p. 22–39.

Gao, G.L., 1989, Review of geological origin about Jinding lead-zinc ore deposit: Earth Science, v. 14, p. 467–475 (in Chinese with English abs.).

——1991, Formation age and involved problems on anhydrite ore in Jinding lead-zinc ore area: Yunnan Geology, v. 2, p. 191–206 (in Chinese with English abs.).

Gleeson, S.A., Wilkinson, J.J., Shaw, H.F., and Herrington, R.J., 2000, Post-magmatic hydrothermal circulation and the origin of base metal mineralization, Cornwall, UK: Journal of the Geological Society, v. 157, p. 589–600.

Goldstein, R., and Reynolds, T.J., 1994, Systematics of fluid inclusions in diagenetic minerals: Society for Sedimentary Geology (SEPM) Short Course, v. 31, 199 p.

Guillong, M.L. Meier, D., Allan, M., Heinrich, C.A., and Yardley, B., 2008, SILLS: A MATLAB-based program for the reduction of laser ablation ICP-MS data of homogeneous materials and inclusions: Mineralogical Association of Canada Short Course, v. 40, p. 328–333.

Gunther, D., Audetat, A., Frischknecht, R., and Heinrich, C.A., 1998, Quantitative analysis of major, minor and trace elements in fluid inclusions using laser ablation inductively coupled plasma mass spectrometry: Journal of Analytical Atomic Spectrometry, v. 13, p. 263–270.

Hammerli, J., Rusk, B., Spandler, C., Emsbo, P., and Oliver, N.H.S., 2013, In situ quantification of Br and Cl in minerals and fluid inclusions by LA-ICP-MS: A powerful tool to identify fluid sources: Chemical Geology, v. 337, p. 75–87.

Hanor, J.S., 1994, Origin of saline fluids in sedimentary basins: Geological Society, London, Special Publications, v. 78, 151 p.

He, L., Song, Y., Chen, K., Hou, Z., Yu, F., Yang, Z., Wei, J., Li, Z., and Liu, Y., 2009, Thrust-controlled, sediment-hosted, Himalayan Zn-Pb-Cu-Ag deposits in the Lanping foreland fold belt, eastern margin of Tibetan Plateau: Ore Geology Reviews, v. 36, p. 106–132.

Heijlen, W., Banks, D.A., Muchez, P., Stensgard, B.M., and Yardley, B.W.D., 2008, The nature of mineralizing fluids of the Kipushi Zn-Cu deposit, Katanga, Democratic Repubic of Congo: Quantitative fluid inclusion analysis using laser ablation ICP-MS and bulk crush-leach methods: Economic Geology, v. 103, p. 1459–1482.

Heinrich, C.A., Ryan, C.G., Mernagh, T.P., and Eadington, P.J., 1992, Segregation of ore metals between magmatic brine and vapor: A fluid inclusion study using PIXE microanalysis: Economic Geology, v. 87, p. 1566–1583.

Heinrich, C.A., Gunther, D., Audetat, A., Ulrich, T., and Frischknecht, R., 1999, Metal fractionation between magmatic brine and vapor, determined by microanalysis of fluid inclusions: Geology, v. 27, p. 755–758.

Heinrich, C.A., Pettke, T., Halter, W.E., Aigner-Torres, M., Audétat, A., Günther, D., Hattendorf, B., Bleiner, D., Guillong, M., and Horn, I., 2003, Quantitative multi-element analysis of minerals, fluid and melt inclusions by laser-ablation inductively-coupled-plasma mass-spectrometry: Geochimica et Cosmochimica Acta, v. 67, p. 3473–3497.

Hou, Z., Zaw, K., Pan, G., Mo, X., Xu, Q., Hu, Y., and Li, X., 2007, Sanjiang Tethyan metallogenesis in S.W. China: Tectonic setting, metallogenic epochs and deposit types: Ore Geology Reviews, v. 31, p. 48–87.

Hu, R., Turner, G., Burnard, P.G., Zhong, H., Ye, Z., and Bi, X., 1998, Helium and argon isotopic geochemistry of Jinding superlarge Pb-Zn deposit: Science in China Series D: Earth Sciences, v. 41, p. 442–448.

Huizenga, J.-M., Gutzmer, J., Banks, D., and Greyling, L., 2005, The Paleoproterozoic carbonate-hosted Pering Zn-Pb deposit, South Africa. II: Fluid inclusion, fluid chemistry and stable isotope constraints: Mineralium Deposita, v. 40, p. 686–707.

Hurtig, N.C., Hanley, J.J., and Gysi, A.P., 2018, The role of hydrocarbons in ore formation at the Pillara Mississippi Valley-type Zn-Pb deposit, Canning basin, Western Australia: Ore Geology Reviews, v. 102, p. 875–893.

Kamenetsky, V.S., van Achterbergh, E., Ryan, C.G., Naumov, V.B., Mernagh, T.P., and Davidson, P., 2002, Extreme chemical heterogeneity of granite-derived hydrothermal fluids: An example from inclusions in a single crystal of miarolitic quartz: Geology, v. 30, p. 459–462.

Kharaka, Y.K., Maest, A.S., Carothers, W.W., Law, L.M., Lamothe, P.J., and Fries, T.L., 1987, Geochemistry of metal-rich brines from central Mississippi Salt Dome basin, U.S.A: Applied Geochemistry, v. 2, p. 543–561.

Klemm, L.M., Pettke, T., Heinrich, C.A., and Campos, E., 2007, Hydrothermal evolution of the El Teniente deposit, Chile: Porphyry Cu-Mo ore deposition from low-salinity magmatic fluids: Economic Geology, v. 102, p. 1021–1045.

Kloppmann, W., Negrel, P., Casanova, J., Klinge, H., Schelkes, K., and Guerrot, C., 2001, Halite dissolution derived brines in the vicinity of a Permian salt dome (N German basin). Evidence from boron, strontium, oxygen, and hydrogen isotopes: Geochimica et Cosmochimica Acta, v. 65, p. 4087–4101.

Kouzmanov, K., Pettke, T., and Heinrich, C.A., 2010, Direct analysis of ore-precipitating fluids: Combined IR microscopy and LA-ICP-MS study of fluid inclusions in opaque ore minerals: Economic Geology, v. 105, p. 351–373.

Kyle, J., and Li, N., 2002, Jinding: A giant Tertiary sandstone-hosted Zn-Pb deposit, Yunnan, China: SEG Newsletter, v. 50, p. 1, 9–16.

Lan, T.G., Hu, R.Z., Fan, H.R., Bi, X.W., Tang, Y.W., Zhou, L., Mao, W., and Chen, Y.H., 2017, In-situ analysis of major and trace elements in fluid inclusion and quartz: LA-ICP-MS method and applications to ore deposits: Acta Petrologica Sinica, v. 33, p. 3239–3262 (in Chinese with English abs.).

Lan, T.G., Hu, R.Z., Bi, X.W., Mao, G.J., Wen, B.J., Liu, L., and Chen, Y.H., 2018, Metasomatized asthenospheric mantle contributing to the generation of Cu-Mo deposits within an intracontinental setting: A case study of the similar to 128 Ma Wangjiazhuang Cu-Mo deposit, eastern North China craton: Journal of Asian Earth Sciences, v. 160, p. 460–489.

Landtwing, M.R., Pettke, T., Halter, W.E., Heinrich, C.A., Redmond, P.B., Einaudi, M.T., and Kunze, K., 2005, Copper deposition during quartz dissolution by cooling magmatic-hydrothermal fluids: The Bingham porphyry: Earth and Planetary Science Letters, v. 235, p. 229–243.

Large, S.J.E., Bakker, E.Y.N., Weis, P., Walle, M., Ressel, M., and Heinrich, C.A., 2016, Trace elements in fluid inclusions of sediment-hosted gold deposits indicate a magmatic-hydrothermal origin of the Carlin ore trend: Geology, v. 44, p. 1015–1018.

Leach, D.L., Sangster, D.F., Kelley, K.D., Large, R.R., Garven, G., Allen, C.R., Gutzmer, J., and Walters, S., 2005, Sediment-hosted lead-zinc deposits: A global perspective: Economic Geology 100th Anniversary Volume, p. 561–607.

Leach, D.L., Bradley, D.C., Huston, D., Pisarevsky, S.A., Taylor, R.D., and Gardoll, S.J., 2010, Sediment-hosted lead-zinc deposits in Earth history: Economic Geology, v. 105, p. 593–625.

Leach, D.L., Song, Y.C., and Hou, Z.Q., 2017, The world-class Jinding Zn-Pb deposit: Ore formation in an evaporite dome, Lanping basin, Yunnan, China: Mineralium Deposita, v. 52, p. 281–296.

Li, C., Liu, X., Zhao, F., Lu, Q., Wu, R., Wang, Y.A., Chu, Y., and Xiao, J., 2011, Actual traces of mantle fluid of Jinding super-large Pb-Zn deposit and the mechanism of crust-mantle overlapping mineralization: Earth Science Frontiers, v. 18, p. 194–206 (in Chinese with English abs.).

Li, X.M., Tan, K.X., Gong, W.J., and Gong, G.L., 2000, Study on the metallogenic epoch of the Jinding lead-zinc deposit with apatite fission track analysis: Geotectonica et Metallogenia, v. 24, p. 282–286 (in Chinese with English abs.).

Liu, H.Q., Bi, X.W., Lu, H.Z., Hu, R.Z., Lan, T.G., Wang, X.S., and Huang, M.L., 2018, Nature and evolution of fluid inclusions in the Cenozoic Beiya gold deposit, SW China: Journal of Asian Earth Sciences, v. 161, p. 35–56.

Liu, J.L., Wang, A.J., Cao, D.H., and Xiu, Q.Y., 2004, Structure and evolution of the postcollisional fault structures in the Three River orogenic belt: Exemplified by the Cenozoic Jianchuan-Lanping basin: Geological Journal of China Universities, v. 12, p. 488–499 (in Chinese with English abs.).

Liu, Y.C., Hou, Z.Q., Yu, Y.S., Tian, S.H., Yang, Z.S., Li, Y.L., and Tian, S.H., 2013, Characteristics and genesis of Lalongla MVT-like deposit in Changdu region, Tibet: Acta Petrologica Sinica, v. 29, p. 1407–1426 (in Chinese with English abs.).

Liu, Y.C., Kendrick, M.A., Hou, Z.Q., Yang, Z.S., Tian, S.H., Song, Y.C., and Honda, M., 2017, Hydrothermal fluid origins of carbonate-hosted Pb-Zn deposits of the Sanjiang thrust belt, Tibet: Indications from noble gases and halogens: Economic Geology, v. 112, p. 1247–1268.

Lowenstein, T.K., Hardie, L.A., Timofeeff, M.N., and Demicco, R.V., 2003, Secular variation in seawater chemistry and the origin of calcium chloride basinal brines: Geology, v. 31, p. 857–860.

Lu, H.Z., Fan, H., Ni, P., Ou, X.G., Sheng, K., and Zhang, W.H., 2004, Fluid inclusion: Beijing, Science Press, 572 p.

Lundegard, P.D., and Trevena, A.S., 1990, Sandstone diagenesis in the Pattani basin (Gulf of Thailand): History of water-rock interaction and comparison with the Gulf of Mexico: Applied Geochemistry, v. 5, p. 669–685.

Luo, J.L., Yang, Y.H., and Zhao, Z., 1994, Evolution of the Tethys in western Yunnan and mineralization for main metal deposits: Beijing, Geological Publishing House, 340 p.

Marsala, A., Wagner, T., and Waelle, M., 2013, Late-metamorphic veins record deep ingression of meteoric water: A LA-ICPMS fluid inclusion study from the fold-and-thrust belt of the Rhenish Massif, Germany: Chemical Geology, v. 351, p. 134–153.

Martel, A.T., Gibling, M.R., and Nguyen, M., 2001, Brines in the carboniferous Sydney Coalfield, Atlantic Canada: Applied Geochemistry, v. 16, p. 35–55.

McCaffrey, M.A., Lazar, B., and Holland, H.D., 1987, The evaporation path of seawater and the coprecipitation of Br^- and K^+ with halite: Journal of Sedimentary Petrology, v. 57, p. 928–937.

McCaig, A.M., Tritlla, J., and Banks, D.A., 2000, Fluid mixing and recycling during Pyrenean thrusting: Evidence from fluid inclusion halogen ratios: Geochimica et Cosmochimica Acta, v. 64, p. 3395–3412.

Meere, P.A., and Banks, D.A., 1997, Upper crustal fluid migration: An example from the Variscides of SW Ireland: Journal of the Geological Society, v. 154, p. 975–985.

Metcalfe, I., 2002, Permian tectonic framework and palaeogeography of SE Asia: Journal of Asian Earth Sciences, v. 20, p. 551–566.

——2013, Gondwana dispersion and Asian accretion: Tectonic and palaeogeographic evolution of eastern Tethys: Journal of Asian Earth Sciences, v. 66, p. 1–33.

Michael, K., Machel, H.G., and Bachu, S., 2003, New insights into the origin and migration of brines in deep Devonian aquifers, Alberta, Canada: Journal of Geochemical Exploration, v. 80, p. 193–219.

Miron, G.D., Wagner, T., Waelle, M., and Heinrich, C.A., 2013, Major and trace-element composition and pressure-temperature evolution of rock-buffered fluids in low-grade accretionary-wedge metasediments, Central Alps: Contributions to Mineralogy and Petrology, v. 165, p. 981–1008.

Mo, X., Deng, J., and Lu, F., 1994, Volcanism and the evolution of Tethys in Sanjiang area, southwestern China: Journal of Southeast Asian Earth Sciences, v. 9, p. 325–333.

Morad, S., Ismail, H.N.B., Deros, L.F., Alaasm, I.S., and Serrhini, N.E., 1994, Diagenesis and formation water chemistry of Triassic reservoir sandstones from southern Tunisia: Sedimentology, v. 41, p. 1253–1272.

Mou, C.L., Wang, J., Yu, Q., and Zhang, L.S., 1999, The evolution of the sedimentary basin in Lanping area during Mesozoic-Cenozoic: Journal of Mineralogy and Petrology, v. 19, p. 30–36 (in Chinese with English abs.).

Munz, I.A., Yardley, B.W.D., Banks, D.A., and Wayne, D., 1995, Deep penetration of sedimentary fluids in basement rocks from southern Norway: Evidence from hydrocarbon and brine inclusions in quartz veins: Geochimica et Cosmochimica Acta, v. 59, p. 239–254.

Najman, Y., Appel, E., Boudagher-Fadel, M., Bown, P., Carter, A., Garzanti, E., Godin, L., Han, J.T., Liebke, U., Oliver, G., Parrish, R., and Vezzoli, G., 2010, Timing of India-Asia collision: Geological, biostratigraphic, and palaeomagnetic constraints: Journal of Geophysical Research—Solid Earth, v. 115, p. 1–18.

Orville, P.M., 1972, Plagioclase ion exchange equilibria with aqueous chloride solutions: Results at 700°C and 2000 bars in the presence of quartz: American Journal of Science, v. 272, p. 234–272.

Pan, G.T., Xu, Q., Hou, Z.Q., Wang, L.Q., Du, D.X., Mo, X.X., Li, D.M., Wang, M.J., Li, X.Z., and Jiang, X.S., 2003, The ore-forming systerm of the orogenic processing in the western "Sanjiang" ploy-arc and the resource estimate: Beijing, Geological Publishing House, 420 p. (in Chinese).

Pelch, M.A., Appold, M.S., Emsbo, P., and Bodnar, R.J., 2015, Constraints from fluid inclusion compositions on the origin of Mississippi Valley-type

mineralization in the Illinois-Kentucky district: Economic Geology, v. 110, p. 787–808.
Pettke, T., Oberli, F., Audetat, A., Guillong, M., Simon, A.C., Hanley, J.J., and Klemm, L.M., 2012, Recent developments in element concentration and isotope ratio analysis of individual fluid inclusions by laser ablation single and multiple collector ICP-MS: Ore Geology Reviews, v. 44, p. 10–38.
Qi, J.H., Li, X., Xu, M., Yi, L., Zhang, Q., Qin, L.M., and Li, K.D., 2018, Origin of saline springs in Yanjing, Tibet: Hydrochemical and isotopic characteristics: Applied Geochemistry, v. 96, p. 164–176.
Qin, G.J., and Zhu, S.Q., 1991, Genetic model and ore prediction in Jinding Pb-Zn deposit: Yunnan Geology, v. 10, no. 2, p. 145–190 (in Chinese with English abs.).
Rabiei, M., Chi, G.X., Normand, C., Davis, W.J., Fayek, M., and Blamey, N.J.F., 2017, Hydrothermal rare earth element (xenotime) mineralization at Maw zone, Athabasca basin, Canada, and its relationship to unconformity-related uranium deposits: Economic Geology, v. 112, p. 1483–1507.
Rauchenstein-Martinek, K., Wagner, T., Walle, M., Heinrich, C.A., and Arlt, T., 2016, Chemical evolution of metamorphic fluids in the Central Alps, Switzerland: Insight from LA-ICPMS analysis of fluid inclusions: Geofluids, v. 16, p. 877–908.
Riley, J.P., and Chester, R., 1971, Introduction to marine chemistry: New York, Academic Press, 465 p.
Roedder, E., 1968, The non-colloidal origin of colloform textures in sphalerite ores: Economic Geology, v. 63, p. 451–471.
——1984, Fluid inclusions: Reviews in Mineralogy, v. 12, p. 1–644.
Rusk, B.G., Reed, M.H., Dilles, J.H., Klemm, L.M., and Heinrich, C.A., 2004, Compositions of magmatic hydrothermal fluids determined by LA-ICP-MS of fluid inclusions from the porphyry copper-molybdenum deposit at Butte, MT: Chemical Geology, v. 210, p. 173–199.
Samson, I.M., and Walker, R.T., 2000, Cryogenic Raman spectroscopic studies in the system NaCl-$CaCl_2$-H_2O and implications for low-temperature phase behavior in aqueous fluid inclusions: The Canadian Mineralogist, v. 38, p. 35–43.
Samson, I.M., Williams-Jones, A.E., Ault, K.M., Gagnon, J.E., and Fryer, B.J., 2008, Source of fluids forming distal Zn-Pb-Ag skarns: Evidence from laser ablation-inductively coupled plasma-mass spectrometry analysis of fluid inclusions from El Mochito, Honduras: Geology, v. 36, p. 947–950.
Sanz-Robinson, J., and Williams-Jones, A.E., 2019, Zinc solubility, speciation and deposition: A role for liquid hydrocarbons as ore fluids for Mississippi Valley-type Zn-Pb deposits: Chemical Geology, v. 520, p. 60–68.
Schlegel, T.U., Waelle, M., Steele-MacInnis, M., and Heinrich, C.A., 2012, Accurate and precise quantification of major and trace element compositions of calcic-sodic fluid inclusions by combined microthermometry and LA-ICPMS analysis: Chemical Geology, v. 334, p. 144–153.
Seo, J.H., Guillong, M., Aerts, M., Zajacz, Z., and Heinrich, C.A., 2011, Microanalysis of S, Cl, and Br in fluid inclusions by LA-ICP-MS: Chemical Geology, v. 284, p. 35–44.
Shi, J.X., Yi, F.H., and Wen, Q.C., 1983, The rock-ore characteristics and mineralization of Jinding lead-zinc deposit, Lanping: Yunnan Geology, v. 2, no 3, p. 179–195 (in Chinese with English abs.).
Shu, Q.H., Chang, Z.S., Hammerli, J., Lai, Y., and Huizenga, J-M., 2017, Composition and evolution of fluids forming the Baivinnuo'er Zn-Ph skarn deposit, northeastern China: Insights from laser ablation ICP-MS study of fluid inclusions: Economic Geology, v. 112, p. 1441–1460.
Simpson, M.P., Strmic Palinkas, S., Mauk, J.L., and Bodnar, R.J., 2015, Fluid inclusion chemistry of adularia-sericite epithermal Au-Ag deposits of the southern Hauraki Goldfield, New Zealand: Economic Geology, v. 110, p. 763–786.
Singer, D.A., 1995, World-class base and precious-metal deposits; a quantitative analysis: Economic Geology, v. 90, p. 88–104.
Smith, M., Banks, D.A., Yardley, B.W.D., and Boyce, A., 1996, Fluid inclusion and stable isotope constraints on the genesis of the Cligga Head Sn-W deposit, SW England: European Journal of Mineralogy, v. 8, p. 961–974.
Smith, M.P., Gleeson, S.A., and Yardley, B.W.D., 2013, Hydrothermal fluid evolution and metal transport in the Kiruna district, Sweden: Contrasting metal behaviour in aqueous and aqueous-carbonic brines: Geochimica et Cosmochimica Acta, v. 102, p. 89–112.
Smith-Schmitz, S.E., and Appold, M.S., 2018, Prediction of ore fluid metal concentrations from solid solution concentrations in ore-stage calcite: Application to the Illinois-Kentucky and Central Tennessee Mississippi Valley-type districts: Geochimica et Cosmochimica Acta, v. 225, p. 210–227.
Song, Y.C., Hou, Z.Q., Yang, T.N., Zhang, H.R., Yang, Z.S., Tian, S.H., Liu, Y.C., Wang, X.H., Liu, Y.X., Xue, C.D., Wang, G.H., and Li, Z., 2011, Sediment-hosted Himalayan base metal deposits in Sanjiang region: Characteristics and genetic types: Acta Petrologica et Mineralogica, v. 30, p. 355–380 (in Chinese with English abs.).
Song, Y.C., Hou, Z.Q., Xue, C.D., and Huang, S.Q., 2020, New mapping of the world-class Jinding Zn-Pb deposit, Lanping basin, southwest China: Genesis of ore host rocks and records of hydrocarbon-rock interaction: Economic Geology, v. 115, p. 981–1002.
Spurlin, M.S., Yin, A., Horton, B.K., Zhou, J., and Wang, J., 2005, Structural evolution of the Yushu-Nangqian region and its relationship to syncollisional igneous activity east-central Tibet: Geological Society of America Bulletin, v. 117, p. 1293–1317.
Steele-MacInnis, M., Bodnar, R.J., and Naden, J., 2011, Numerical model to determine the composition of H_2O-NaCl-$CaCl_2$ fluid inclusions based on microthermometric and microanalytical data: Geochimica et Cosmochimica Acta, v. 75, p. 21–40.
Steele-MacInnis, M., Ridley, J., Lecumberri-Santhez, P., Schlegel, T.U., and Heinrich, C.A., 2016, Application of low-temperature microthermometric data for interpreting multicomponent fluid inclusion compositions: Earth-Science Reviews, v. 159, p. 14–35.
Stoffell, B., Wilkinson, J.J., and Jeffries, T.E., 2004, Metal transport and deposition in hydrothermal veins revealed by 213 nm UV laser ablation microanalysis of single fluid inclusions: American Journal of Science, v. 304, p. 533–557.
Stoffell, B., Appold, M.S., Wilkinson, J.J., McClean, N.A., and Jeffries, T.E., 2008, Geochemistry and evolution of Mississippi Valley-type mineralizing brines from the Tri-State and Northern Arkansas districts determined by LA-ICP-MS microanalysis of fluid inclusions: Economic Geology, v. 103, p. 1411–1435.
Stueber, A.M., and Walter, L.M., 1991, Origin and chemical eolution of formation waters from Silurian-Devonian strata in the Illinois basin, USA: Geochimica et Cosmochimica Acta, v. 55, p. 309–325.
Stueber, A.M., Saller, A.H., and Ishida, H., 1998, Origin, migration, and mixing of brines in the Permian basin: Geochemical evidence from the eastern Central basin platform, Texas: American Association of Petroleum Geologists, AAPG Bulletin, v. 82, p. 1652–1672.
Tang, Y.Y., 2013, Abnormal enrichment mechanisms of ore-forming metals in the Jinding Zn-Pb deposit, Yunnan Province, China: Unpublished Ph.D. thesis: Beijing, The University of Chinese Academy of Sciences, 129 p. (in Chinese with English abs.).
Tang, Y.Y., Bi, X.W., He, L.P., Wu, L.Y., Feng, C.X., Zou, Z.C., Tao, Y., and Hu, R.Z., 2011, Geochemical characteristics of trace elements, fluid inclusions and carbon-oxygen isotopes of calcites in the Jinding Zn-Pb deposit, Lanping, China: Acta Petrologica Sinica, v. 27, p. 2635–2645 (in Chinese with English abs.).
Tang, Y.Y., Bi, X.W., Wu, L.Y., Zou, Z.C., and He, L.P., 2013, Carbon, oxygen, strontium and lead isotopic geochemistry in the Jinding super-large Zn-Pb deposit, Yunnan Province: Geochimica, v. 42, p. 467–480 (in Chinese with English abs.).
Tang, Y.Y., Bi, X.W., Fayek, M., Hu, R.Z., Wu, L.Y., Zou, Z.C., Feng, C.X., and Wang, X.S., 2014, Microscale sulfur isotopic compositions of sulfide minerals from the Jinding Zn-Pb deposit, Yunnan Province, Southwest China: Gondwana Research, v. 26, p. 594–607.
Tang, Y.Y., Bi, X.W., Fayek, M., Stuart, F.M., Wu, L.Y., Jiang, G.H., Xu, L.L., and Liang, F., 2017, Genesis of the Jinding Zn-Pb deposit, northwest Yunnan Province, China: Constraints from rare earth elements and noble gas isotopes: Ore Geology Reviews, v. 90, p. 970–986.
Tao, X.F., Zhu, L.D., Liu, D.Z., Wang, G.Z., and Li, Y.G., 2002, The formation and evolution of the Lanping basin in western Yunnan: Journal of Chengdu University of Technology, v. 29, p. 521–525 (in Chinese with English abs.).
Tapponnier, P., Lacassin, R., Leloup, P.H., Scharer, U., Zhong, D.L., Wu, H.W., Liu, X.H., Ji, S.C., Zhang, L.S., and Zhong, J.Y., 1990, The Ailao Shan Red River metamorphic belt—Tertiary left-lateral shear between Indochina and South China: Nature, v. 343, p. 431–437.
Teng, Y.G., Liu, J.D., Zhang, C.J., Ni, S.J., and Peng, X.H., 2000, Geological and geochemic information of deep ore fluid in Lanping basin, Yunnan Province: Contributions to Geology and Mineral Resources Research, v. 4, p. 314–319 (in Chinese with English abs.).
Third Geological Team, 1984, The exploration report of the Jinding Zn-Pb deposit in Lanping County, Yunnan Province: Yunnan Bureau of Geology and Mineral Resources, p. 50–106 (in Chinese).
Ulrich, M.R., and Bodnar, R.J., 1988, Systematics of stretching of fluid inclusions 2: Barite at 1 atm confining pressure: Economic Geology, v. 83, p. 1037–1046.

Ulrich, T., Gunther, D., and Heinrich, C.A., 2001, The evolution of a porphyry Cu-Au deposit, based on LA-ICP-MS analysis of fluid inclusions: Bajo de la Alumbrera, Argentina: Economic Geology, v. 96, p. 1743–1774.
Wagner, T., Fusswinkel, T., Walle, M., and Heinrich, C.A., 2016, Microanalysis of fluid inclusions in crustal hydrothermal systems using laser ablation methods: Elements, v. 12, p. 323–328.
Wang, A.J., Cao, D.H., Gao, L., Wang, G., Guan, Y., Xiu, Q., and Liu, J., 2009, A probe into the genesis of Jinding super-large lead-zinc ore deposit: Acta Geologica Sinica, v. 83, p. 43–54 (in Chinese with English abs.).
Wang, J.H., Yin, A., Harrison, T.M., Grove, M., Zhang, Y.Q., and Xie, G.H., 2001, A tectonic model for Cenozoic igneous activities in the eastern Indo-Asian collision zone: Earth and Planetary Science Letters, v. 188, p. 123–133.
Wang, Q.F., Deng, J., Li, C.S., Li, G.J., Yu, L., and Qiao, L., 2014, The boundary between the Simao and Yangtze blocks and their locations in Gondwana and Rodinia: Constraints from detrital and inherited zircons: Gondwana Research, v. 26, p. 438–448.
Wang, X.C., Zhou, X., Zheng, Y.H., Song, C., Long, M., Chen, T., Ren, Z.H., Yang, M.L., Li, X.L., and Guo, J., 2017, Hydrochemical characteristics and mixing behavior of thermal springs along the Bijiang River in the Lanping basin of China: Environmental Earth Sciences, v. 76, p. 1–19.
Wen, C.Q., Cai, J.M., Liu, W.Z., Qin, G.J., and Chen, S.F., 1995, Geochemical characteristics of fluid inclusions in the Jinding lead-zinc deposit, Yunnan: China Journal of Mineralogy and Petrology, v. 15, no. 4, p. 79–84 (in Chinese with English abs.).
Wenz, Z.J., Appold, M.S., Shelton, K.L., and Tesfaye, S., 2012, Geochemistry of Mississppi-type mineralizing fluids of the Ozark Plateau: A regional synthesis: American Journal of Science, v. 312, p. 22–80.
Wilkinson, J.J., 2010, A review of fluid inclusion constraints on mineralization in the Irish ore field and implications for the genesis of sediment-hosted Zn-Pb deposits: Economic Geology, v. 105, p. 417–442.
——2014, Sediment-hosted zinc-lead mineralization: Processes and perspectives, *in* Holland, H.D., and Turekian, K.K., eds., Treatise on geochemistry, 2nd ed.: Oxford, Elsevier, p. 219–249.
Wilkinson, J.J., Stoffell, B., Wilkinson, C.C., Jeffries, T.E., and Appold, M.S., 2009, Anomalously metal-rich fluids form hydrothermal ore deposits: Science, v. 323, p. 764–767.
Williams-Jones, A.E., Samson, I.M., Ault, K.M., Gagnon, J.E., and Fryer, B.J., 2010, The genesis of distal zinc skarns: Evidence from the Mochito deposit, Honduras: Economic Geology, v. 105, p. 1411–1440.
Wilson, T.P., and Long, D.T., 1993, Geochemistry and isotope chemistry of Michigan basin brines—Devonian formations: Applied Geochemistry, v. 8, p. 81–100.
Worden, R.H., Manning, D.A.C., and Bottrell, S.H., 2006, Multiple generations of high salinity formation water in the Triassic Sherwood sandstone: Wytch Farm oilfield, onshore UK: Applied Geochemistry, v. 21, p. 455–475.
Wu, G.G., and Wu, X.D., 1989, A preliminary study on the tectonic evolution and mineralization regularity of the Jinding lead-zinc deposit, Yunnan Province: Earth Science, v. 14, p. 477–486 (in Chinese with English abs.).
Wu, H., Boulter, C.A., Ke, B., Stow, D.A.V., and Wang, Z., 1995, The Changning-Menglian suture zone; a segment of the major Cathaysian-Gondwana divide in Southeast Asia: Tectonophysics, v. 242, p. 267–280.
Xue, C.J., Chen, Y.C., Wang, D.H., Yang, J.M., Yang, W.G., and Zeng, R., 2003, Geology and isotopic composition of helium, neon, xenon and metallogenic age of the Jinding and Baiyangping ore deposits, northwest Yunnan, China: Science in China Series D—Earth Sciences, v. 46, p. 789–800.
Xue, C.J., Zeng, R., Liu, S.W., Chi, G.X., Qing, H.R., Chen, Y.C., Yang, J.M., and Wang, D.H., 2007, Geologic, fluid inclusion and isotopic characteristics of the Jinding Zn-Pb deposit, western Yunnan, South China: A review: Ore Geology Reviews, v. 31, p. 337–359.
Xue, C.J., Chi, G.X., and Fayek, M., 2015, Micro-textures and in situ sulfur isotopic analysis of spheroidal and zonal sulfides in the giant Jinding Zn-Pb deposit, Yunnan, China: Implications for biogenic processes: Journal of Asian Earth Sciences, v. 103, p. 288–304.
Yalikun, Y., Xue, C., and Symons, D.T.A., 2017, Paleomagnetic age and tectonic constraints on the genesis of the giant Jinding Zn-Pb deposit, Yunnan, China: Mineralium Deposita, v. 53, p. 1–15.
Yang, T.N., Ding, Y., Zhang, H.R., Fan, J.W., Liang, M.J., and Wang, X.H., 2014, Two-phase subduction and subsequent collision defines the Paleotethyan tectonics of the southeastern Tibetan Plateau: Evidence from zircon U-Pb dating, geochemistry, and structural geology of the Sanjiang orogenic belt, southwest China: Geological Society of America Bulletin, v. 126, p. 1654–1682.
Yardley, B.W.D., 2005, 100th anniversary special paper: Metal concentrations in crustal fluids and their relationship to ore formation: Economic Geology, v. 100, p. 613–632.
Ye, Q.T., Hu, Y.Z., and Yang, Y.Q., 1992, Regional geochemistry background and the gold-silver-lead-zinc mineralization in Sanjiang area: Beijing, Geological Publishing House, 264 p. (in Chinese).
Yin, A., and Harrison, T.M., 2000, Geologic evolution of the Himalayan-Tibetan orogen: Annual Review of Earth and Planetary Sciences, v. 28, p. 211–280.
Yunnan Bureau Geological Mineral Resource, 1990, Regional geology of Yunnan Province: Beijing, Geology Publishing House, 729 p. (in Chinese).
Zeng, P., Li, H., Li, Y., Wang, Z., Wen, L., and Siwen., L., 2016, Asian largest lead-zinc ore deposit: The Jinding giant Pb-Zn deposit by three stages superimposed mineralization: Acta Geologica Sinica, v. 90, p. 2384–2397.
Zhang, C.J., Ni, S.J., Teng, Y.G., Peng, X.H., and Liu, J.D., 2000, Relationship between Himalayan tecotonomagmatic movement and mineralization in Lanping basin, Yunnan Province: Journal of Mineralogy and Petrology, v. 20, p. 35–39 (in Chinese with English abs.).
Zhao, X.Y., 1989, On the genesis of the Jinding lead-zinc ore deposit in Yunnan: Earth Science, v. 14, no. 5, p. 523–530 (in Chinese with English abs.).
Zhao, Z., 2007, the Jinding Pb-Zn deposit of Lanping—a land facies sedex ore deposit: Yunnan Geology, v. 26, p. 1–14 (in Chinese with English abs.).
Zou, Z.C., Hu, R.Z., Bi, X.W., Wu, L.Y., Zhang, J.R., Tang, Y.Y., and Li, N., 2016, Noble gas and stable isotopic constraints on the origin of the Ag-Cu polymetallic ore deposits in the Baiyangping area, Yunnan Province, SW China: Resource Geology, v. 66, p. 183–198.
Zwart, E.W., and Touret, J.L.R., 1994, Melting behavior and composition of aqueous fluid inclusions in fluorite and calcite-appilcation within the system H_2O-$CaCl_2$-NaCl: European Journal of Mineralogy, v. 6, p. 773–786.

Lan Mu is a Ph.D. student at the Institute of Geochemistry, Chinese Academy of Sciences. She earned her B.Sc. degree in geology from the Central South University in 2015. Her research focuses on investigation of detailed fluid evolution and metallogenesis of low-temperature hydrothermal deposits by in situ microanalysis (e.g., EPMA, LA-(MC)-ICP-MS). Currently she works on sediment-hosted Zn-Pb deposits in the Sanjiang region, southeast Tibet Plateau.